Accepted Manuscript

Stiffness memory of indirectly 3D-printed elastomer nanohybrid regulates chondrogenesis and osteogenesis of human mesenchymal stem cells

Linxiao Wu, Adrián Magaz, Tao Wang, Chaozong Liu, Arnold Darbyshire, Marilena Loizidou, Mark Emberton, Martin Birchall, Wenhui Song

PII: S0142-9612(18)30644-6

DOI: 10.1016/j.biomaterials.2018.09.013

Reference: JBMT 18884

To appear in: *Biomaterials*

Received Date: 21 June 2018

Revised Date: 28 August 2018

Accepted Date: 8 September 2018

Please cite this article as: Wu L, Magaz Adriá, Wang T, Liu C, Darbyshire A, Loizidou M, Emberton M, Birchall M, Song W, Stiffness memory of indirectly 3D-printed elastomer nanohybrid regulates chondrogenesis and osteogenesis of human mesenchymal stem cells, *Biomaterials* (2018), doi: 10.1016/j.biomaterials.2018.09.013.

Stiffness memory of indirectly 3D-printed elastomer nanohybrid regulates chondrogenesis and osteogenesis of human mesenchymal stem cells

Authors: Linxiao Wu[1], Adrián Magaz[1†], Tao Wang[1,2], Chaozong Liu[3], Arnold Darbyshire[1], Marilena Loizidou[1], Mark Emberton[1], Martin Birchall[4], Wenhui Song[1*]

Affiliations:
[1]Centre for Biomaterials in Surgical Reconstruction and Regeneration, Division of Surgery & Interventional Science, University College London, London, United Kingdom

[2]Precision Medical Centre, the Seventh Affiliated Hospital of Sun Yat-Sen University, Shenzhen 518107, China

[3]Institute of Orthopaedics and Musculoskeletal Science, Division of Surgery & Interventional Science, University College London, London, United Kingdom

[4]UCL Ear Institute, Royal National Throat, Nose and Ear Hospital, University College London, London, United Kingdom

* Corresponding author, email: w.song@ucl.ac.uk

† Current address: Bio-Active Materials Group, School of Materials, The University of Manchester, Manchester, UK

Abstract: The cellular microenvironment is dynamic, remodeling tissues lifelong. The biomechanical properties of the extracellular matrix (ECM) influence the function and differentiation of stem cells. While conventional artificial matrices or scaffolds for tissue engineering are primarily static models presenting well-defined stiffness, they lack the responsive changes required in dynamic physiological settings. Engineering scaffolds with varying elastic moduli is possible, but often lead to stiffening and chemical crosslinking of molecular structure with limited control over scaffold architecture. A family of indirectly 3D printed elastomeric nanohybrid scaffolds with thermoresponsive mechanical properties that soften by inverse self-assembling at body temperature have been developed recently. The initial stiffness and subsequent stiffness relaxation of the scaffolds regulated the proliferation and differentiation of human bone-marrow derived mesenchymal stem cells (hBM-MSCs) towards the chondrogenic and osteogenic lineages over 4 weeks, as measured by immunohistochemistry, histology, ELISA and qPCR. hBM-MSCs showed enhanced chondrogenic differentiation on softer scaffolds and osteogenic differentiation on stiffer ones, with similar relative expression to that of human femoral head tissue. Overall, stiffness relaxation favored osteogenic activity over chondrogenesis *in vitro*.

Keywords
Stiffness memory, stem cell differentiation, chondrogenesis, osteogenesis, 3D printing, elastomer nanohybrid

1. Introduction

In vitro studies do not fully recapitulate the native tissue environment [1]. Living tissues constantly remodel throughout life; they are dynamic systems [2] with markedly distinct biomechanical features that are subject to change during the course of development or during disease progression [3]. In particular, the extracellular matrix (ECM) plays a crucial role in governing organ branching during tissue regeneration. It not only provides structural integrity for tissue elasticity [4], but many ECM components are locally synthesized and continuously reorganize to modulate diverse cellular processes. In this sense, dynamic conditions have been identified as an important regulator in tissue development [5]. A dynamic environment plays an important role in translating the biomechanical signals to the cells and can dramatically affect their behaviour via regulation of gene expression [6]. Indeed, cellular behaviours such as motility [7–10], migration [10–13], proliferation [12,13], stem cell differentiation [8,14,15], and pathological behavior [16], have been shown to be driven by changes in matrix stiffness. However, conventional synthetic scaffolds, implants or coatings are often designed and manufactured without considering how to adapt to the dynamic changes during the implantation. Those implants are primarily static with well-defined and stable stiffness that lacks the dynamic biological nature required to undergo changes in substrate elasticity, decisive in several cellular processes during tissue development and wound healing.

Human mesenchymal stem cells (MSCs) reside in tissues of varying stiffness and participate in tissue regeneration with their stiffness changing as the repairing tissue matures and remodels [6]. This suggests that stem cells in different states may respond differentially as they commit to a specific fate, and apart from sensing their current environment, stem cells are affected by memory of their mechanical history [17–20]. For instance, human bone-marrow derived mesenchymal stem cells (hBM-MSC) cultured on soft or stiff hydrogels and later transferred to substrates of opposite stiffness [20] switched from neurogenic differentiation towards osteogenic lineages, whilst MSCs that were transferred from stiff to soft substrates retained elevated osteogenesis markers.

Stimulus-responsive polymers change their structure, physical or chemical properties, in response to various external stimuli. These may be chemical (e.g. hydrolysis [21], addition of divalent cations [22,23] or delivery of single-stranded DNA oligomers [24–27]), thermal [28], pH-dependent [29], photo-sensitive [19,30], or magnetic [17,31–33]. Such responsive materials, mainly hydrogels, have been developed recently [34–37] and applied to study temporal stiffening [17,22–33] and softening [19,21] effects of the substrate on cells both in 2D and 3D cell cultures. For example, Guvendering and Burdich studied the effects of a hydrogel whose stiffness increases by light-mediated crosslinking in the presence of hBM-MSCs [2]: stiffening at an earlier stage led to osteogenic differentiation, while stiffening at later times led to an equally mixed osteogenic/adipogenic fate. Yang *et al.* investigated the use of ultraviolet radiation to soften a hydrogel through photo-degradation and the mechanical memory of hBM-MSCs during culture [19] based on the expression of the transcriptional activator Yes-associated protein (YAP). YAP was found to be activated in the nucleus of MSCs cultured on stiff substrates while it deactivated and relocated to the cytoplasm when cells were cultured on soft substrates instead. They demonstrated that by softening a stiff hydrogel at different culturing times, YAP-transit to the nucleus affected cellular “memory”. Abdeen *et al.* used a magneto-activated gel to study the effects of varying substrate elasticity on hMSC differentiation [17]. They showed how a magnetic field could modulate cell spreading and cytoskeletal tension via changes in the matrix

stiffness, with an impact on the secretion of proangiogenic molecules by hMSCs. Cells exhibited osteogenic activity when cultured on soft substrates whose matrix stiffness was magnetically increased at later time points. Independently controlling both composition and elasticity of a substrate is difficult, and also limits the range of stiffness achieved through changing a hydrogel's physico-chemistry [38]. In addition, these settings present several limitations, from short-term stability issues to problems with cytocompatibility [39,40]. Moreover, nearly all above strategies lead to an increased dynamic stiffening of the substrate; little work has been performed on the effect of stiffness softening of cell-seeded substrates.

A family of thermoresponsive "stiffness memory" non-degradable poly(urea-urethane) (PUU) nanohybrid scaffolds with stiffness relaxation properties at body temperature towards their intrinsic elasticity through inverse self-assembling have been recently developed using 3D printing guided thermal induced phase transition (3D-TIPS) [41]. These PUU nanohybrid based bespoke scaffolds can be indirectly 3D printed through 3D-TIPS approach, with versatile control of scaffold architecture and physico-mechanical properties. The scaffolds with different initial stiffness were achieved through microphase separation of PUU chains and crystallisation of soft segments at different thermal processing conditions of 3D-TIPS. It was found that, regardless the different initial stiffness, these scaffolds "remembered" to relax to their intrinsic hyperelasticity at rubber phase when subjected to body temperature near the phase transition, i.e. the melting point of crystalline domains of soft segments. Herein, the tuneable compression mechanical properties and stiffness relaxation of these scaffolds have been characterised, based on differential initial stiffnesses and hierarchical porous structure. The effects of stiffness softening on differentiation of hBM-MSCs with reference to chondrogenic and osteogenic lineages have been systematically investigated.

2. Materials and Methods

2.1 Fabrication and characterization of the scaffolds

2.1.1 Design and fabrication of elastomer nanohybrid scaffolds using an indirect printing 3D-TIPS technique

PUU-POSS elastomer nanohybrid solution was synthesized as needed using a previously described protocol [42]. PUU-POSS scaffolds were then produced by 3D-TIPS, a 3D guided thermal induced phase-separation of the polymeric solution within 3D printed poly(vinyl alcohol) (PVA) preforms, used as water soluble sacrificial moulds [41]. Three scaffold groups with different mechanical properties and porous structures were produced by the 3D-TIPS technique at different thermal processing conditions (**Table 1**): cryo-coagulation (CC), cryo-coagulation and heating (CC+H), and room temperature coagulation and heating (RTC+H), as described in [41]. At each 3D-TIPS process condition, a group of the scaffolds was fabricated with increasing infill densities (30-80%) respectively.

Table 1 3D-TIPS processing

Scaffolds	**PUU-POSS solution filled PVA preform**	**Coagulation conditions**	**Thermal treatment**
Room temperature coagulation +heating, RTC+H	Room temperature, 25°C	Room temperature, 25°C water for 24 h	40°C water for 24 h

Cyro-coagulation, CC	–20°C for 24 h	0°C ice water for 24 h	No thermal treatment
Cryo-coagulation +heating, CC+H	–20°C for 24 h	0°C ice water for 24 h	40°C water for 3 h

2.1.2 Physico-mechanical characterization of the scaffolds

The top surface and cross sectional views of dried scaffolds with various infill densities were examined using an optical microscope (Olympus DSX500,UK) and a field emission scanning electron microscope (Zeiss Supra 35VP FE-SEM, Germany).

For compression mechanical testing, cuboids (preform size of 30mm x 30mm x 30mm) of each scaffold group (n=6) were fabricated. Compression mechanical properties of the scaffolds before and after incubation at 37.5 °C up to 28 days were tested at wet condition using an Instron 5655 tester (Instron Ltd., USA) with a 500N load cell.

Dynamic mechanical properties of the scaffolds (length 15 mm, width 6.5 mm, thickness 2 mm; n=2) were tested in compression modes at day 0 and after day 28, in a bioreactor at 37.5 °C in water using an ElectroForce Biodynamic® Test Instrument 5160 (TA, USA) with a 200N load cell. The samples were loaded with a sinusoidal ramp of constant frequency of 1 Hz with a controlled strain (25%) at increasing cycles up to 200,100 cycles per sample.

The porosity of PUU-POSS scaffolds was calculated using the equation below,

$$\rho = (1 - \frac{d_a}{d_b}) \times 100\%$$

Where the bulk density (d_b) of PUU-POSS was taken as 1.15x10^{-6} g/cm^3 (1150 kg/m^3), and the apparent density (d_a) was calculated using the weight (g) and volume (cm^3) of each sample. Six polymer discs (of diameter 1.6 cm) were cut from each scaffold using a pre-shaped cutter. Average radius and height were measured for each disc to the nearest 0.01 mm using a digital caliper.

A KRÜSS DSA 100 (KRÜSS GmbH) system was used for static water contact angle measurements of samples (n=20), using a sessile drop method. Sterile deionized water (diH_2O) was used as a solvent, with a droplet volume of 3 µL. One droplet per samples and 20 samples (5 mm in diameter) were analyzed.

2.2 *In vitro* experiments

2.2.1 Protein adsorption (BCA assay)

Total serum protein adsorption on the scaffolds was determined by a BCA assay kit (Pierce, Rockford IL, USA) using BSA standards in PBS (Sigma-Aldrich Limited, Gillingham, USA). Briefly, scaffolds (n=4 replicates) were incubated with complete growth medium at 37.5°C for 24 hrs. The medium was removed before transferring the scaffolds to another 48-well plate. Scaffolds were washed three times with PBS before adding the BCA reagent to each well and were left for incubation for 2 hrs at 37°C. The absorbance was then measured at 562 nm using a microplate reader (Anthos 2020, 288 BioChrome Ltd, UK).

2.2.2 Expansion, cell seeding and differentiation of hBM-MSCs

Human bone-marrow derived mesenchymal stem cells (hBM-MSCs; Sciencell™, California, USA) were subcultured and expanded with mesenchymal stem cell medium (MSCM; Sciencell™, California, USA) in a T75 flask (**Figure D1** in Data in Brief [43]). Before seeding, hBM-MSCs were washed with PBS and trypsinized with 3 mL of 0.25% trypsin-EDTA (Life-technologies, Paisley, UK) after PBS being aspirated. Cells were incubated at 37°C for 3 min and dislodged with gentle flask-tapping. Trypsin was neutralized with 7 mL of fresh MSCM and the cell suspension was transferred to a 15 mL tube; spun at 1,200 rpm for 5 min. After centrifugation, the concentrated cell pellet was resuspended in 2 mL of fresh MSCM and a viable cell count was performed by means of a Trypan Blue exclusion assay and a haemocytometer chamber.

Polymer discs (11 mm diameter and 3 mm thickness) were cut from the fabricated PUU-POSS scaffolds with 50% infill density. Samples (n=7 replicates) were sterilised in 70% ethanol and stirred for 30 minutes before being washed four times in sterile PBS. All discs placed in 48-well plates were pre-incubated in 500 µl of MSCM for 24 hrs overnight. Each scaffold was then seeded at a density of 9×10^4 cells/cm^3, corresponding 2.5×10^4 cells/scaffold (2^{nd} passage) in 500 µl of MSCM based on a preliminary 10-day study evaluating metabolic activity of the scaffolds at different cell-seeding densities.

Media was replaced every three days, and the metabolic activity of cells was monitored on days 1, 3, 7, 10 and 14 to determine cell viability through alamarBlue® (AB) (Serotec Ltd, Kidlington, Oxford, UK) testing. At each day point, Total DNA content was also quantified using a fluorescent Hoechst 33258 stain. Tissue culture plate (TCP) was used as comparison.

Chondrogenic differentiation was carried out on day 1 post-seeding. Briefly, MSCM was discarded and replaced with 1 mL of mesenchymal stem cell chondrogenic differentiation medium (MCDM) supplemented with 10% of mesenchymal stem cell chondrogenic differentiation supplement (MCDS) (Sciencell™, California, USA), 5% penicillin/streptomycin (Sciencell™, California, USA), and 10 ng/mL TGF-β3, (differentiation inducer) (Miltenyi Biotec Ltd., Surrey, UK). Medium was replaced every third day of culture according to the manufacturer's instructions throughout a 4-week culture. PUU-POSS scaffolds (n=4) were collected at days 1, 7, 14, 21, 28 and 35.

Osteogenic differentiation was carried out on day 1 post-seeding. Briefly, MSCM was discarded and replaced with 1 mL of mesenchymal stem cell osteogenic differentiation medium (MODM) supplemented with 10% of mesenchymal stem cell osteogenic supplement (MODS) (Sciencell™, California, USA). Medium was replaced every second day of culture according to the manufacturer's instructions throughout a 4-week culture. PUU-POSS scaffolds (n=4) were collected at days 1, 7, 14, 21 and 28.

Human dermal fibroblast (HDF) cells served as negative control of differentiation. Spheroids were used as positive control of differentiation: $1x10^6$ cells were centrifuged and the cell pellet placed in the incubator at 37°C in a humidified atmosphere of 95% air and 5% CO_2; spheroids formed within 24 h. Spheroids were used as a positive control to demonstrate the success of the differentiation protocol and were compared with the differentiation of hBM-MSCs on the fabricated scaffolds. In addition, human femoral head (HFH) was used as positive control for comparison to native mature osteo/chondrocytes. HFH was collected from patients (with written consent) undergoing total knee replacement surgery at the Royal National Orthopaedic Hospital, approved by the UK Health Research Authority (REC reference: 15/LO/2052).

Cell-laden scaffolds (n=4) after *in vitro* differentiation were also subjected to compressive mechanical testing following the same procedure as outlined above.

2.2.3 Morphology of cell-seeded scaffolds

Cell-laden scaffolds (n=2) after osteogenesis and chondrogenesis were were stored in a vial containing primary fixative solution, 4% paraformaldehyde (PFA) and 2% glutaraldehyde in a 0.1 M cacodylate buffer at pH 7.4 and 4ºC over night. Samples were washed thereafter three times with phosphate buffered saline (PBS) and then three times with bi-distillated water so as fixatives' residues could be completely removed. Samples were then dehydrated through a series of graded ethanol solutions. Gradually, water was replaced with an intermediate medium (ethanol) starting from a concentration of 10–50% (v/v). At this time, the incubation time was 10 min for each solution. Samples were then infiltrated in sequence with a solution of 70% ethanol (v/v) for 10 min; 95%, and 100% (v/v) ethanol were exchanged three times and let with an incubation time of 10 min (each step). In the end, samples were stored in propylene oxide 10 min in a sealed dish.

Based on the method of critical point drying (CPD) upon CO_2 phase transition, the samples were transferred into the chamber of a CPD machine (CPD 030, BAL-TEC, Schalksmuehle, Germany) so as to ensure that the cells were continuously immersed in 100% ethanol. The system was slowly cooled down to 10°C (typically 1°C/step). The ethanol was gradually replaced with CO_2 liquid. This consist of typically 10 ethanol/CO_2 exchange repetitions. Then, the chamber's temperature was increased by 1°C/step until reaching a temperature of about 40°C. At the critical temperature and pressure, the CO_2 liquid turns into the supercritical state, and the samples in the chamber completely dry off. Finally, the supercritical CO_2 can be released via a control valve by a temperature increase.

Samples were mounted on a typical electron microscopy stub using a double-adhesive carbon tape. Each sample was coated with a thin layer of sputtering deposition by a sputter gold coater (15–30 s deposition time, 15 mA current) (SC500 EMScope). Samples were observed with a field emission scanning electron microscope (Zeiss Supra 35VP FE-SEM) by fixing a voltage of 3kV.

2.2.4 Immunohistochemistry analysis

Cell-laden scaffolds were washed in diH_2O before being fixed in 4% (w/v) PFA in PBS. The samples were permeabilised with 0.1% triton x-100 (Sigma, UK) and non-specific binding of primary antibody was inhibited by incubation with 3% BSA (Sigma, UK) in PBS. They were then incubated with either 1/100 mouse anti-Collagen1 polyclonal antibody (Abcam, Cambridge, UK), 1/100 rabbit anti-Collagen 2 polyclonal antibody (Abcam, Cambridge, UK), 1/100 rabbit anti-SOX9 polyclonal antibody (Abcam, Cambridge, UK) or 1/100 mouse monoclonal anti-Aggrecan (Abcam, UK) in 3% BSA in PBS for 2 h at room temperature. Adjacent sections were incubated with Immunoglobulin G (IgG) antibody as negative controls. A 1/500 goat anti-mouse Alexafluor®-594, 1/500 goat anti-rabbit Alexafluor®-647 secondary antibody or 1/500 goat anti-rabbit Alexafluor®-555 secondary antibody (Molecular Probes, UK) in 1% BSA in PBS was added for 1 h at room temperature followed by counterstaining with phalloidin Alexafluor®-488 (Sigma, UK), respectively, to counterstain for F-actin. Finally, samples were stained with DAPI (Sigma, UK). 1/500 OsteoSense 680 EX (NEV10020EX, perkinelmer, USA) was used for staining as marker of calcium.

An alizarin red staining assay was performed according to the manufacturer's instructions to look at calcium deposition. Briefly, after 21 days in osteogenic medium, cell-laden polymer discs were fixed with 4 % PFA in PBS, washed twice with diH_2O and stained with 1% Alizarin red S (ARS, pH 4.2) for 20 min at room temperature. Excess stain was washed away with two changes of diH_2O.

Images were taken using a confocal microscope (Leica TCS SP8vis) with x10 and x20 water immersion objective lens. Z-stacking images were acquired by scanning 9 point areas (3x3) throughout 1mm thickness of the scaffold at 7 μm/Z-step. Image stacks were visualized and analyzed using ImageJ software (San Diego, US), and 3D reconstructions were compiled from 428 imaged sections (each of 7 μm thickness).

2.2.5 Quantitative analysis of sulfated glycosaminoglycans (sGAG)

The ratio of sGAGs/DNA was quantified over a 4-week period by means of a Blyscan™ sulphated glycosaminoglycan assay (Biocolor Ltd.; Antrim, UK). DNA concentrations were calculated using the fluorescent dye Hoechst 33258 binding assay (Sigma-Aldrich, UK) and Total DNA levels measured for normalization purposes. 0.5 mL of 0.25% trypsin-EDTA (Life-technologies, Paisley, UK) were added into each scaffold type (n=6). Extracted cell suspensions of 250 μL and 1 mL of Blyscan dye reagent (Sigma-Aldrich, UK) were transferred to micro-centrifuge tubes, which were placed on a gentle mechanical shaker for 30 minutes. During this period, sGAG-dye complex would form and precipitate out from the soluble unbound dye. The tubes were later spun at 12,000 rpm for 10 min and the supernatant was carefully removed. 0.5 mL of dissociation reagent was added to the pellet with interval mixing in vortex to help resuspend the sGAG-dye complex. Finally, 200 μL of each suspension was transferred to a clear 96-well plate and the absorbance was read at 630 nm using a microplate reader (Biotek; Swindon, UK). For comparison, GAG content was normalized to DNA content.

2.2.6 Gene expression via quantitative reverse transcriptase polymerase chain reaction (qPCR) analysis

Multipotent and differentiated cells in each scaffold were used for mRNA sample preparation. Cells on the scaffolds (n=4) were dissociated using TrypLE after removing the culture medium, incubated at 37^{o}C for 3 min and harvested into 15 mL tubes. They were then centrifuged at 800 ×g for 3 min and the cell pellets were used for total RNA extraction using a Qiagen RNeasy mini-kit (Qiagen, UK). A high-capacity RNA-to-cDNA™ kit (Life Technologies, UK) was used for reverse transcription.

Genes related to chondrogenic differentiation (*SOX9*, *COL2A1*, *COLX* and *ACAN*) and osteogenic differentiation (*ALP*, *COL1A1*, *RUNX2*, *SPP1*, *BGLAP*, *SP7*) were analyzed by qPCR analysis over a period of 28 and 21 days respectively. Expression of the house-keeping gene GAPDH served for normalization [44].

2.2.7 ELISA analysis

Enzyme-linked immunosorbent assay (ELISA) was used to detect chondrogenesis presence of Aggrecan, Collagen II and glycosaminoglycan (GAG) content in 3D scaffolds (n=3) within their cell culture medium at weeks 2, 3 and 4. Osteogenesis presence of Osteocalcin and Collagen I was also detected at weeks 1, 2 and 3. ELISA kits used were human COL2 ELISA kit (Abbexa; Cambridge UK), human GAGs ELISA kit (Abbexa; Cambridge UK), human Aggrecan ELISA (Abcam, UK), human osteocalcin quantikine ELISA Kit (R&D System, UK) and COL1 ELISA

Kit (antibodies-online, UK). Optical density was determined using a microplate reader (Anthos 2020 microplate reader; Biochrome Ltd, UK). All experiments were carried out in triplicate.

2.2.8 Histological analysis

Differentiated hBM-MSCs on the various PUU-POSS scaffold groups (n=2) (days 21 or 28) were fixed in 4% PFA in saline buffer. Briefly, cell-laden samples were embedded in paraffin wax and cut into 4 μm thick sections using a rotary microtome, Leica RM2235 (Leica Microsystem Ltd., Milton Keynes, UK). Slide sections were then deparaffinised and stained with haematoxylin and eosin (H&E) stains, to indicate gross cell morphology.

Cartilage-like ECM production was investigated using Alcian Blue (A-Blue) staining for polysaccharide indication (e.g. glycosaminoglycans), Masson's trichrome (MT) staining for collagen indication, and antibody collagen II (COL2) staining for collagen II production. Osteocyte-like ECM production was investigated using Alizarin red S (ARS) staining for calcium indication, and antibody collagen I (COL1) staining for collagen I production.

2.2.9 Element detection by EDX analysis

Scanning electron microscopy (Carl Zeiss, Germany, CrossBeam XB 1540 FIB-SEM) with an Energy Dispersive X-Ray Spectroscopy (EDX) detector (EDAX Inc.) was used to analyze elemental surface regions of composition of the scaffolds (n=3) for detection of calcium (Ca) and phosphorous (P), as well as the relative distribution of these elements. A human femoral head bone-cartilage joint was used as control.

2.2.10 Quantitative analysis of mineralization

The area of mineralization, as stained with Alizarin red (ARed-Q, Sciencell™, California, USA), was quantified using ImageJ (NIH, USA) of bright field images. In brief, images were converted to a binary grayscale, a threshold was set to highlight only stained areas and the area was measured. In addition, the amount of ARS extracted from the samples was quantified by the method of Gregory et al.[45]. Absorbance was measured at 520 nm with a microplate reader (Anthos 2020 microplate reader; Biochrome Ltd, UK).

2.2.11 Quantitative measurement of ALP activity

Alkaline Phosphatase (ALP) activity was measured using stable p-nitrophenol phosphate substrate by Alkaline Phosphatase Assay Kit (Colorimetric) (Merck; Millipore; USA). At each time point over a 3-week period, culture medium was removed by decantation and cells were washed with PBS and harvested in 1 mL universal ALP buffer (Merck; Millipore; USA). Cells were sonicated twice for 20 sec and centrifuged at 3,000 rpm for 5 min at 4°C. ALP activity in the supernatants was determined following addition of p-nitrophenyl phosphate substrate and the reaction was stopped using 100 µl of 0.1 N NaOH. The optical density was measured at 405 nm using a microplate reader (Spectra Max Plus 384 MK3, Thermo, UK). The ALP activity was calculated from a standard curve after normalization to total protein content, which was measured using the Bradford protein assay kit (Pierce, Rockford, IL, USA). ALP experiments were repeated twice with n=5 for each substrate.

2.3 Statistical analysis

Statistical analysis of the results was performed using Graph-Pad Prism 6 (GraphPad Software San Diego, USA). Statistical significance was calculated by one-way (for analyzing one independent variables) or two-way (for comparisons across more than two independent

variables) analysis of variance (ANOVA) using Tukey's post hoc test, or two-tailed unpaired Student's t tests (for parametric data, where comparing data between two groups). A value of $p<0.05$ was considered statistically significant. Distribution testing showed that all data was parametrically distributed.

3 Results

3.1 Thermoresponsive "stiffness memory" of elastomeric nanohybrid scaffolds

A family of thermoresponsive inorganic POSS nanocage terminated PUU elastomeric nanohybrid scaffolds with a digitally defined complex shape have been developed recently [41]. These have hierarchical interconnected porous network fabricated by thermal-induced phase separation of the nanohybrid solution within 3D printed water soluble polyvinyl alcohol (PVA) sacrificial moulds (3D-TIPS) [41]. Three types of thermoresponsive "stiffness memory" scaffolds were developed by varying the coagulation temperature and post-thermal treatment: cryo-coagulation (CC group), cryo-coagulation and heating (CC+H group), and room temperature coagulation and heating (RTC+H) (**Table 1**). The scaffolds demonstrated controllable initial tensile mechanical properties and stiffness softening to their intrinsic rubbery phase corresponding to the nanophase structure regardless their processing condition. CC scaffolds with the highest tensile modulus possessed the most pronounced stiffness softening at body temperature, attributed to a phase transition of melting and subsequent reverse self-assembling from a semicrystalline ordered structure to a quasi-random nanophase crossing over a wide range of chain relaxation times. CC and CC+H groups have a wider range of porous structures from the macro- to nano-scale generated during the cryo-coagulation process, compared to RTC+H samples [41].

As physiological exemplar, the stress and loading range of a common human activity, kneeling, is referenced in this study. Here, the stiffness softening behavior of the scaffolds with different infill density at physiological-relevant compression loading conditions were characterized. **Figure 1** shows structures, compression mechanical properties of the scaffolds with different infill densities and processing conditions, and isothermal stiffness softening of 50% infill density scaffolds during incubation at 37°C. **Figure 1A** and **1B** show hierarchical interconnected porous structures of 3D-TIPS scaffolds with digitally defined macro-pores to micro- to nano-pores generated during phase separation of polymer solution. SEM images of cross section of 50CC in **Figure 1B** demonstrate a bead-like network of pores with diameters ranging from a few microns to nanometres generated during the cryo-process. Mercury porosimetry measurements revealed the pore size and distribution of the scaffold with 50% infill density [41] and data were analysed in **Figure D2** and **Table D4** in Data in Brief [43]. The 50CC scaffold group consisted of the widest range of size distribution ranging from 400 to 3nm, with the highest surface area (58.5 m^2/g) among the three groups due to the slow phase separation during the cryo-process. 50CC+H scaffolds had a similar bead-stacking morphology and pore size distribution, with fewer pores at 10 µm - 3 nm and reduced surface area (24.5 m^2/g), owing to shrinkage during post thermal treatment. 50RTC+H scaffolds had a narrow distribution of pore sizes from 400 to 10 µm with the least surface area (4.6 m^2/g). SEM images show an irregular surface with a minimal number of open nano-pores (**Figure 1B**) due to faster diffusion and phase separation at room temperature and shrinkage during post thermal treatment, resulting in the formation of a dense surface with fewer pores. As expected, variations in the infill density dramatically affected the compression mechanical properties of the scaffolds, with significantly ($p<0.05$) greater compression modulus and strength for high infill densities due to less digitally defined macro porous structure (**Figure**

1, and **Tables D1-D2** in Data in Brief [43]). Cryo-coagulation also substantially increased the compression modulus and strength due to the formation of semi-crystalline ordered structures within the CC scaffolds, compared to CC+H and RTC+H with thermal treatment [41].

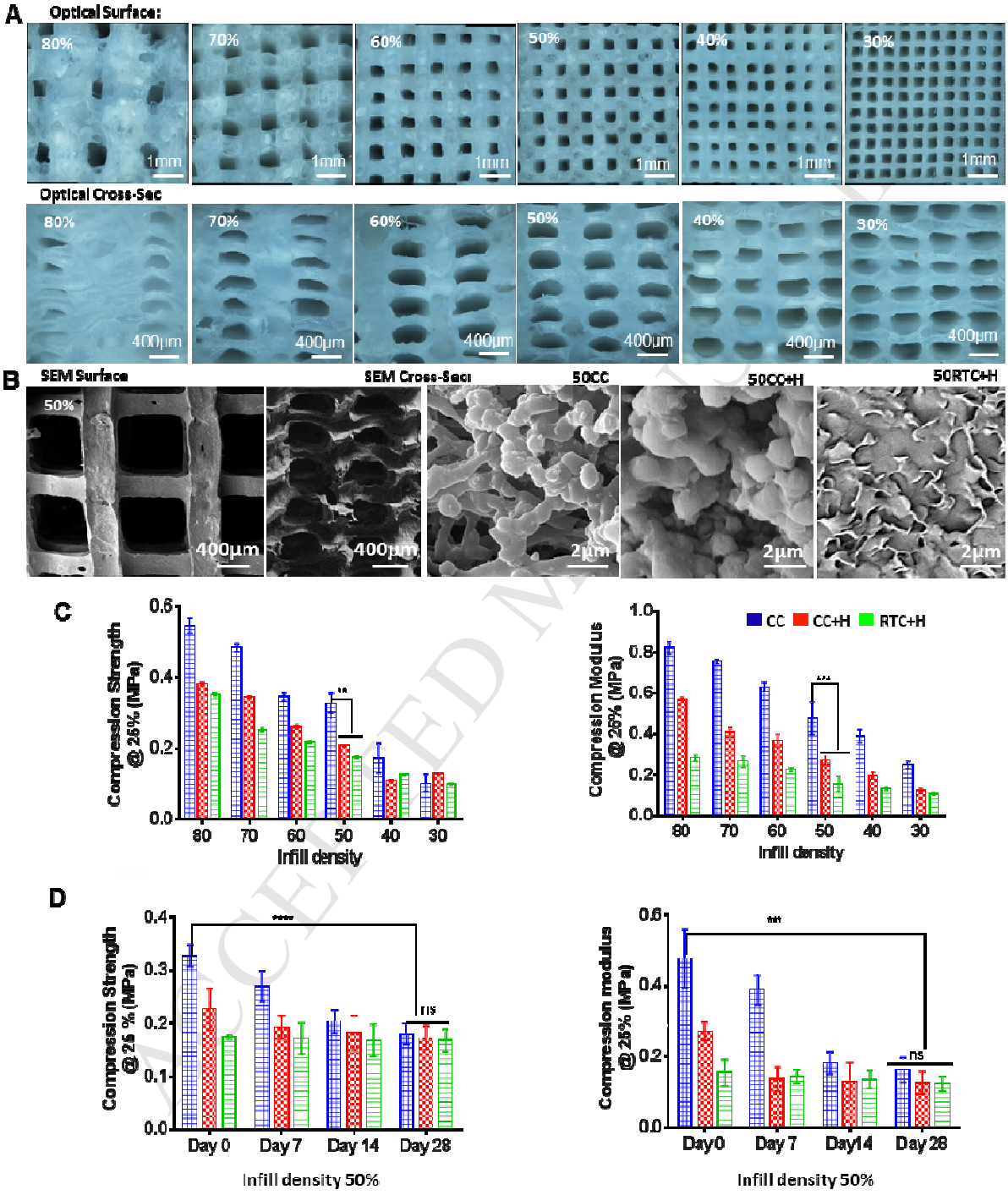

Figure 1 Stiffness softening of PUU-POSS scaffolds under compression. (A) Optical images of surface and cross-section of the scaffolds with infill densities 80-30% made by 3D-TIPS. (B) SEM images of surface and cross-sections of PUU-POSS scaffolds with 50% infill density. (C)

Compression mechanical properties of the scaffolds with various infill densities under different processing conditions. (D) Compression mechanical properties of scaffolds with a 50% infill density during incubation at 37°C over a 28-day period. **p<0.01; ***p<0.001.

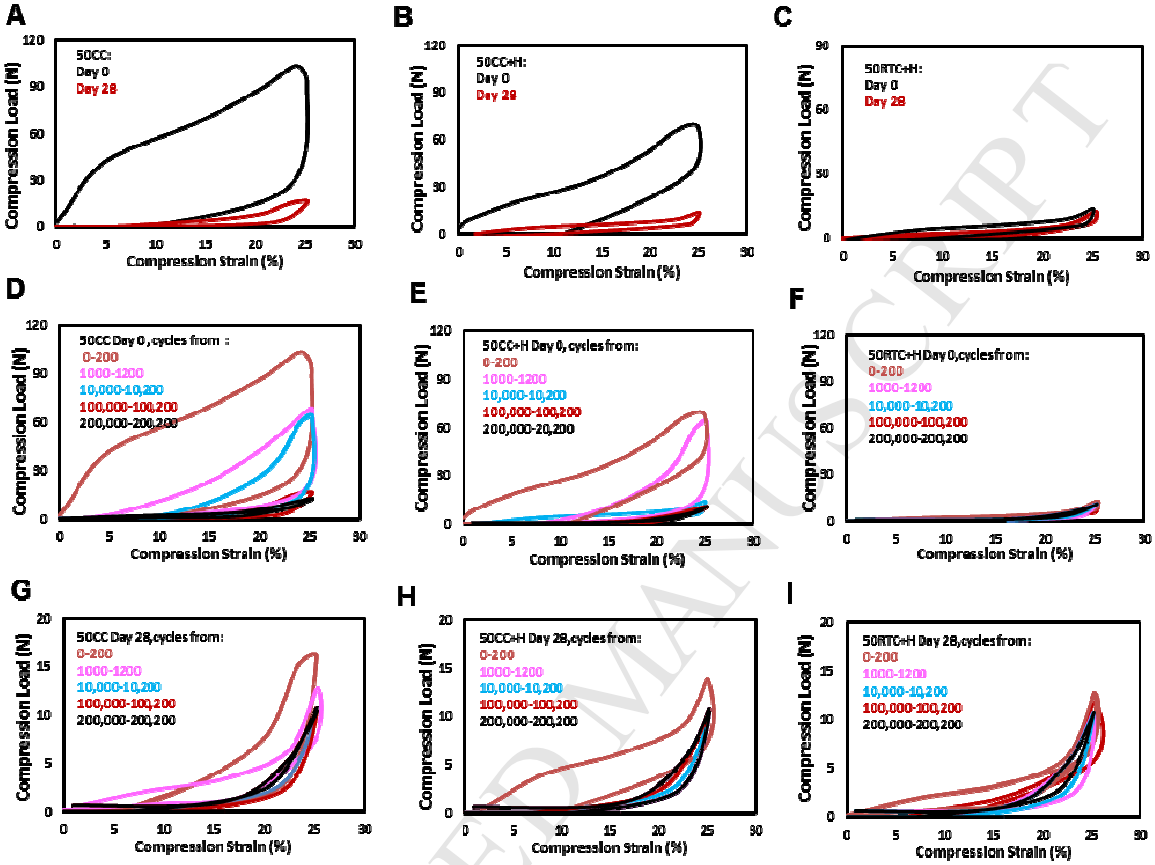

Figure 2 Stiffness softening of PUU-POSS scaffolds with a 50% infill density under cyclic compression. (A-C) Cyclic compression loading profile of scaffolds at 0-200 cycles before and after 28 days. (D-F) Dynamic compression loading profile of scaffolds at increasing cycles at day 0. (G-I) Dynamic compression loading profile of scaffolds at increasing cycles at day 28.

The similar isothermal stiffness softening of 50% infill CC (50CC) scaffolds was observed in the compression test at cell culture condition (i.e. 37°C). **Figure 1 C** shows that both the compression modulus and strength of the 50CC and 50CC+H scaffolds gradually reduced, with 54% and 48% reduction in the compression modulus, and 38% and 18.2% reduction in the compression strength for 50CC and 50CC+H respectively in the first 14 days of incubation at 37 °C, and then reached a similar level to that of the 50RTC+H group by 28 days (p-value non-significant) (**Table D2** in Data in Brief [43]). The stiffness softening and hyperelasticity of the scaffolds was also clearly magnified by reduction of the cyclic loading (i.e. 200 cycles) before and after isothermal relaxation at 37°C for 28 days (**Figure 2 A-C**). All samples displayed reduced hysteresis values and gradually established by reaching their intrinsic elasticity after compression cyclic loading or isothermal annealing (**Table D3** in Data in Brief [43]). 50CC

scaffolds demonstrated the largest area of hysteresis loop as produced, but gradually became softer with increasing reversible compliance through reduction of the loss energy under lower compression stress after 28-day's incubation. In contrast, the 50RTC+H scaffolds did not change significantly after 28 day's incubation, showing almost similar reversible hyperelasticity as produced under much lower cyclic load. 50CC+H scaffolds showed a smaller scale of stiffness softening, with only a trace of hysteresis loop indicating residual inelastic energy after isothermal annealing.

The dynamic response of the scaffolds was further evaluated at increasing cycles (**Figure 2 D-I**). Typical hysteresis of stress and strain loops and changes in their configuration appeared when 50CC scaffolds were subjected to higher cyclic stresses for over 2×10^6 times at 37°C (**Figure 2 D**). A slow stress damping and reduction of hysteresis loop area was measured at increasing number of cycles in response to the transitions from 3D order semi-crystalline to quasi-random nanophase structures observed in the 50CC sample. In contrast, soft rubbery 50RTC+H scaffolds displayed highly reversible entropic hyperelasticity under low cyclic load, about x6 lower, compared to 50CC and 50CC+H scaffolds on day 0 (**Figure 2 E-F**). The strain variation curves were superimposed and could rapidly return to its original form with full recovery during decrement of the load in a co-phasal way with the least hysteresis and energy loss. 50CC+H scaffolds also showed reversible stress-strain characteristics, with only a trace of hysteresis loop indicating inelastic energy residual after thermal treatment process. After 28 days incubation, a similar dynamic loading test at increasing cycles for over 2×10^6 times at 37.5°C was carried out; all scaffolds exhibited similar entropic elastic behavior confirming once more the "stiffness memory" effect of the scaffolds (**Figure 2 G-I**).

3.2 "Stiffness memory" effect on proliferation of hBM-MSCs

hBM-MSCs cells were seeded on the scaffolds, and their ability to attach and proliferate were assessed over a 14-day period (**Figure 3**). The 50CC and 50CC+H scaffolds showed a lower contact angle (**Figure 3 A**) and greater amount of protein adsorption (**Figure 3 B**) (p-value non-significant between them) compared to the 50RTC+H group ($p<0.01$), which may be attributed to the aforementioned hierarchical porous structures and resulting in a large surface area of the scaffolds (i.e. CC and CC+H) by cryo-3D-TIPS process (**Figure 1 A-B, Figure D2** and **Table D4** in Data in Brief [43]). The static contact angle measured is determined by the surface chemistry and the surface roughness of the membrane. PUU-POSS is a hydrophobic polymer in nature. Uniform micro- to nano porous structure on the surface of 50CC and 50CC+H appeared to act as capillary to absorb water, thus reducing the contact angle. The smaller pores of 50CC, the higher their capillary effect contributed to faster water absorption, thus decreasing the contact angle with decreasing pore sizes and increasing protein adsorption [46]. hBM-MSCs were found to be initially more metabolically active and proliferate faster ($p<0.01$) on softer 50CC+H scaffolds compared to the rigid 50CC group; however, following cellular viability and proliferation assays after a 10-day period, non-significant differences could be observed as the stiffness softening was occurring (**Figure 3 C-D**). The morphology of hBM-MSCs showed flat cell bodies and long actin spindles on all three scaffolds (**Figure 3 E-J**). Confocal microscopy at days 1 and 10 (**Figure 3 H-I**) confirmed cellular activity within 50CC scaffolds as seen by immunofluorescent staining, and 3D reconstructions of fluorescent intensity demonstrated constant increase in cell density across the full thickness of the scaffold.

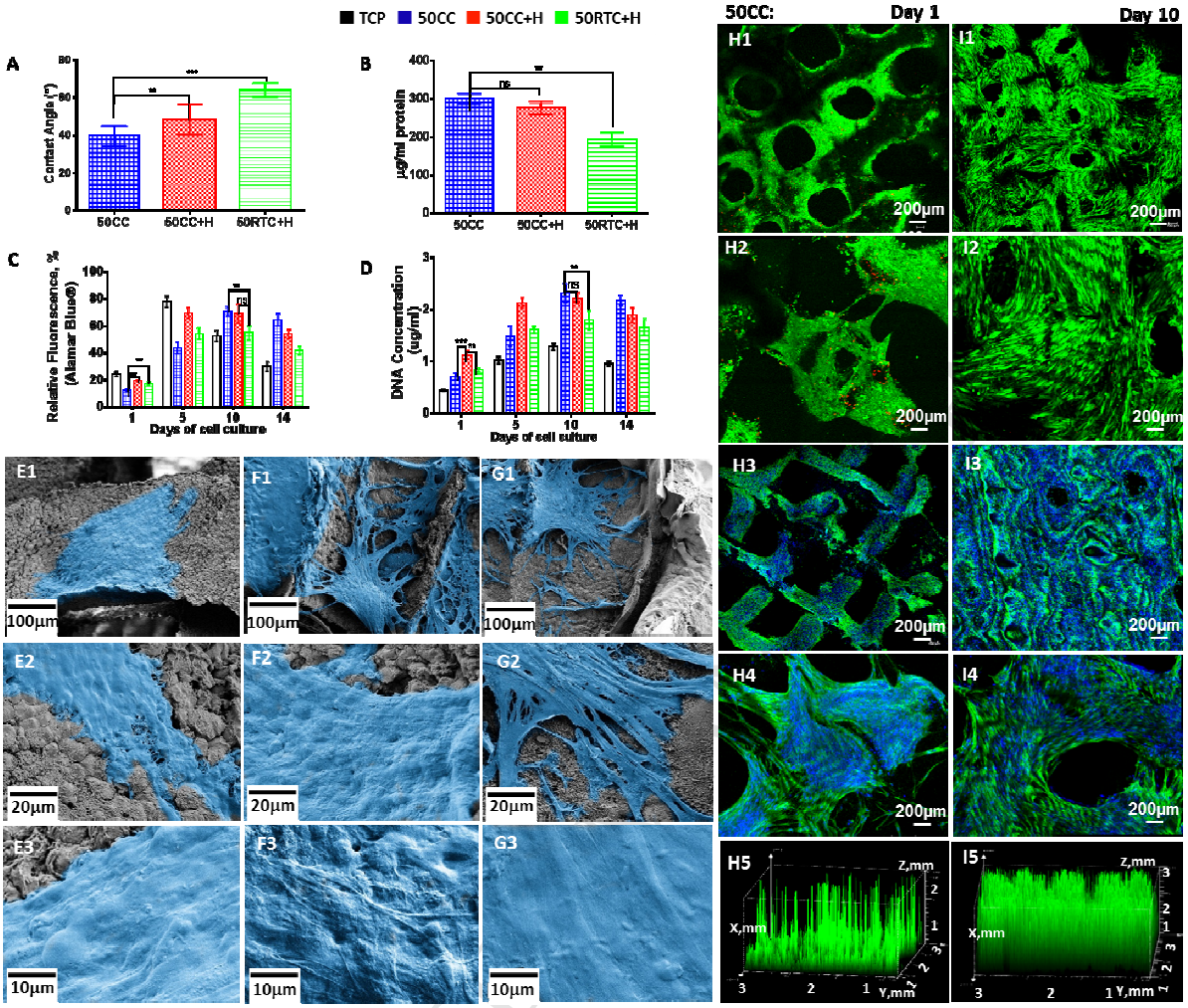

Figure 3 Cellular proliferation of hBM-MSCs on the various 50% infill 3D printed nanohybrid elastomer scaffolds during stiffness softening. (A) contact angle; (B) protein adsorption; (C) alamarBlue fluorescence assay®; (D) Total DNA analysis (n=6); (E-G) SEM images showing cell attachment at day 5 for (E) 50CC, (F) 50CC+H, and (G) 50RCT+H. (H-I) Live (green) - dead (red) staining, and F-actin (green) with nuclei counterstained (blue) as shown by confocal microscopy at days 1 and 10 for 50CC scaffolds, along with 3D reconstructions of fluorescent light intensity.**p<0.01; ***p<0.001.

3.3 "Stiffness memory" effect on *in vitro* chondrogenesis of hBM-MSCs

hBM-MSCs were cultured with chondrogenic medium for differentiation towards the chondrogenic lineage, and RNA was collected over a 4-week period. Chondrocyte-like mesenchymal cells are presented by strong positivity for Collagen II (green) and Aggrecan (red) deposition on the 50CC+H group at day 28 as seen under confocal microscopy, followed by the CC scaffold with reduced Aggrecan deposition and the least on the 50RTC+H sample (**Figure 4 A-F**). The gene expression of cartilage associated ECM formation was quantified by qPCR. Gene expression of chondrogenic associated genes *ACAN, SOX9, COL2A1 and COLX* increased with culture time in all scaffold groups (**Figure 4 G-L**). Although all groups featured stimulated

chondrogenic differentiation, results suggested higher chondrogenic associated gene expression in 50CC+H scaffolds ($p<0.05$) compared to 50CC and 50RTC+H groups. In fact, non-significant differences for all genes tested on the 50CC+H scaffold were observed at week 4 when compared to human femoral head (HFH) used as control (**Figure 4 K**). In addition, the amount of glycosaminoglycan production as sGAG/DNA (**Figure 4 L**) increased over time within all scaffold groups; in particular, sGAG/DNA level reached and maintained the highest at week 4 for the 50CC+H group, significantly higher ($p<0.01$), compared to the rest of the groups and the spheroids as positive control. Compared to HFH, non-significant differences were found at week 4 with respect to the 50CC+H scaffold. It is also noted that the difference of associated gene expression between 50CC and 50CC+H was gradually reduced during stiffness relaxation.

Presence of GAG, Aggrecan and Collagen II released to the medium was further quantified by ELISA (**Figure 4 M-O**). The highest expression of GAG, Aggrecan and Collagen II was detected on the 50CC+H group at all day points compared to the rest of the groups ($p<0.05$), and non-significant differences were found at week 3 with respect to HFH suggesting full maturation on such scaffold. While the values quantified for the 50CC group were lower than those for the 50CC+H group, it was still significantly higher than the 50RTC+H group. Overall, this data suggests that the 50CC scaffold, and the 50CC+H group in particular, led to a more rapid effect in induction of chondrogenesis within hBM-MSCs. These results were further corroborated by histological staining at week 4 (**Figure 5, Figure D3** in Data in Brief [43]). Increased cellular penetration into the scaffold, alongside deposition of Collagen II and proteoglycan components of the extracellular matrix associated with chondrocytes were observed in 50CC+H and 50CC scaffold groups. Chondrocyte-like mesenchymal cells were embedded in a chondrocyte-like matrix presenting the typical cartilage pericellular lacunae more evident on the 50CC+H sample, strongly evident at higher magnification, relative to the spheroid control and human femoral head cartilage. EDX mapping of the scaffolds was also carried out to evaluate calcium and phosphorus distribution across the samples (**Figure 6 A**, **Figure D4 A** and **Table D5** in Data in Brief [43]). As expected for chondrogenesis, results confirmed low presence of both elements in the engineered tissue on all groups; in particular, 0.67 wt% P and 0.92wt % Ca were quantified on the 50CC+H scaffold, similar to human femoral head cartilage (**Figure 6 A, Figure D4 C** in Data in Brief [43]).

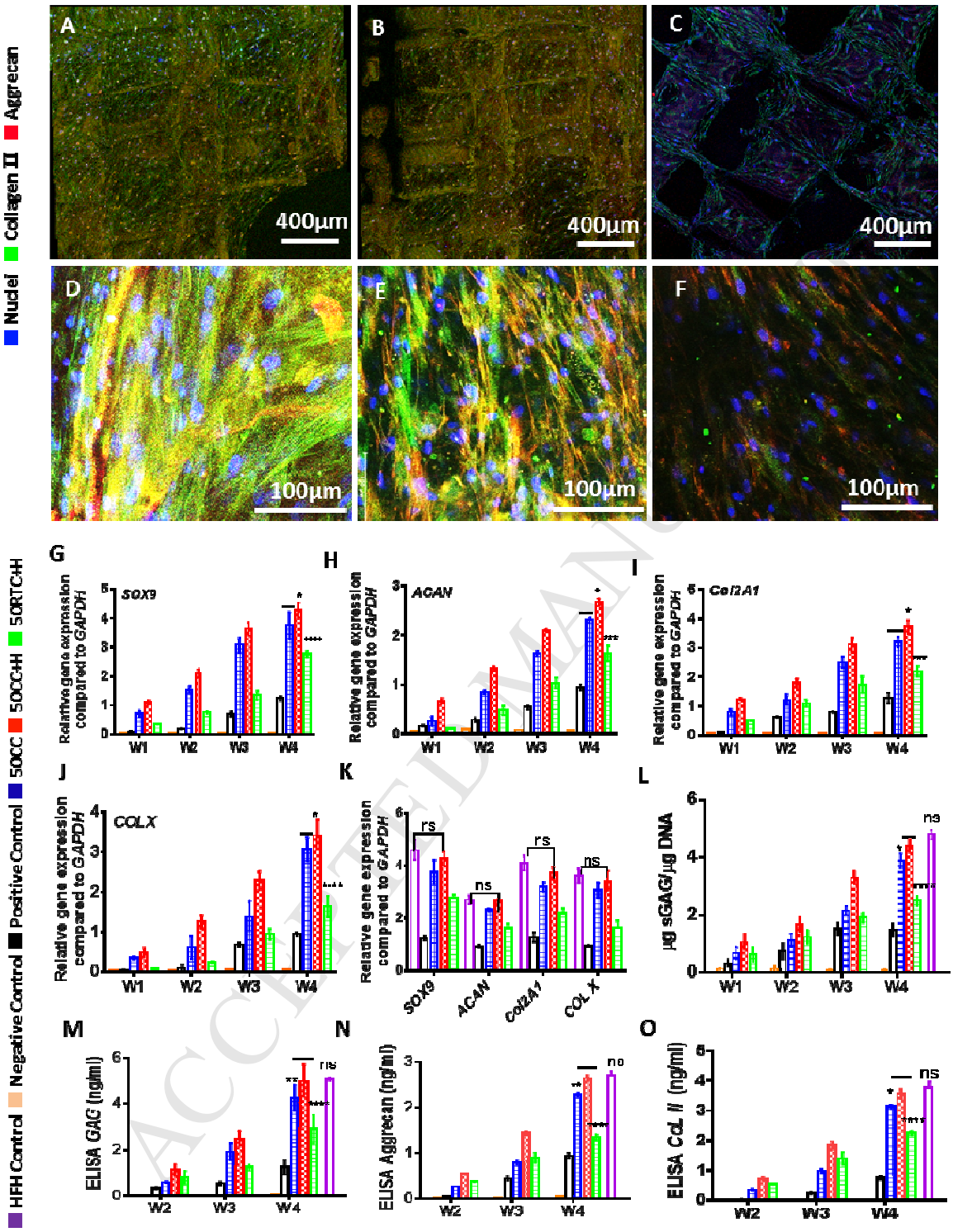

Figure 4 Chondrogenic differentiation on 50% infill elastomer nanohybrid scaffolds during stiffness softening. (A-F) Confocal microscopy of hBM-MSC under chondrogenic conditions at two different magnifications: chondrogenic differentiation after 4 weeks for (A, D) 50CC, (B, E) 50CC+H and 50RT+H (C, F) showing Collagen II (green), Aggrecan (red) and cell nuclei (blue). (G-J) Chondrogenic differentiation of hBM-MSCs quantified by qPCR during a 4-week period:

(G) chondrogenic *SOX9* (transcription factor SOX9) expression; (H) chondrogenic *ACAN* (Aggrecan) expression; (I) chondrogenic *COL2A1* (Collagen II) expression; and (J) chondrogenic *COLX* (Collagen X) expression. (K) Comparison of quantitative analysis of gene expression at week 4 with human femoral head. (L) Quantitative analysis of synthesis of sulfated glycosaminoglycans µgGAG/µgDNA over a 4-week period compared to human femoral head. (M-O) ELISA analysis for presence of GAG, Aggrecan and Collagen II secretion to the medium at weeks 2, 3 and 4. The mean of triplicate wells is plotted, and the error bars represent SD. *p<0.05; **p<0.01; ***p<0.001; ****p<0.0001; "-" represents the reference to which the p-value is compared.

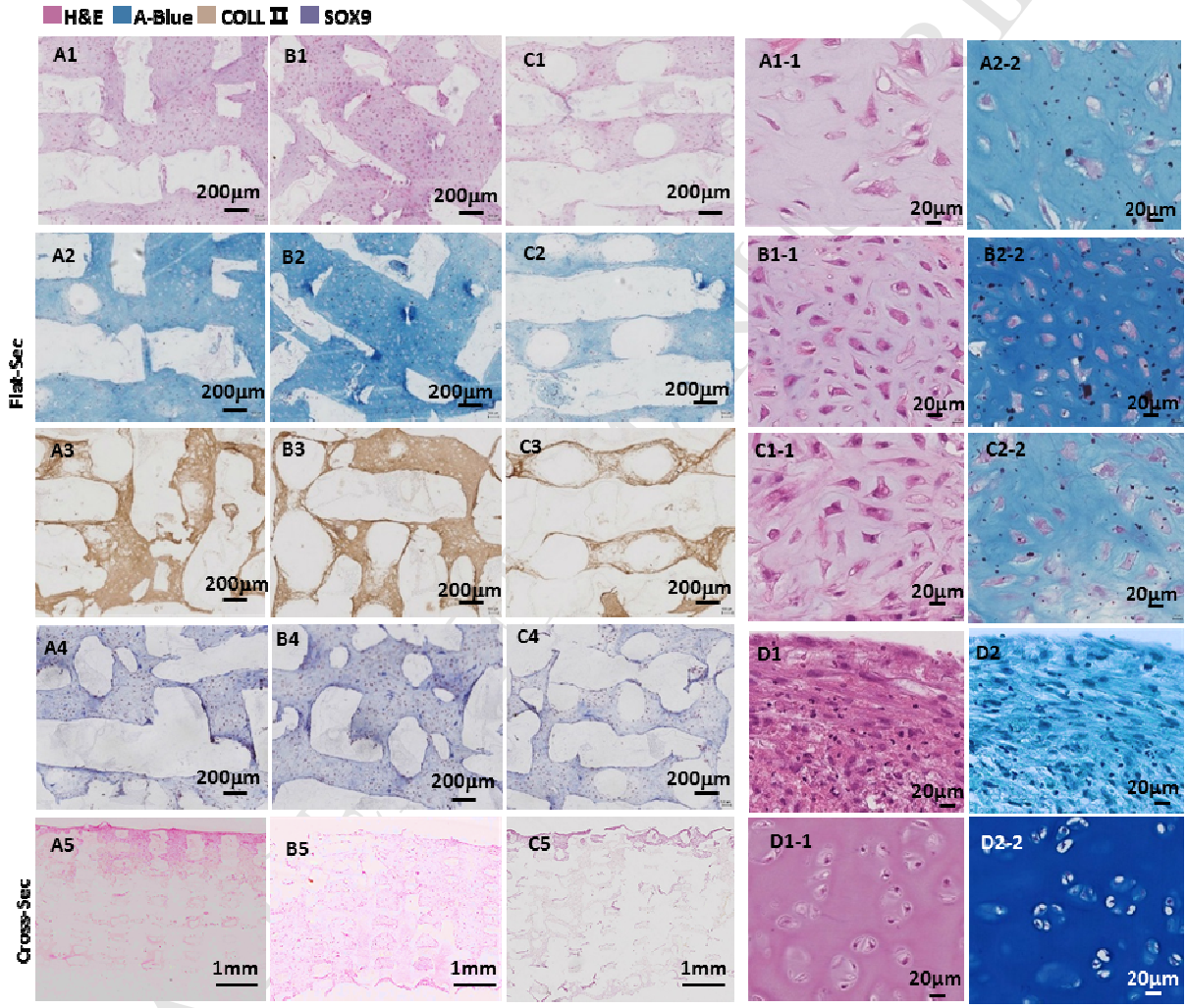

Figure 5 Histological analysis of chondrogenic differentiation on 50% infill elastomer nanohybrid scaffolds during stiffness relaxation. At week 4 in plane-sections for (A1-A4) 50CC, (B1-B4) 50CC+H, and (C1-C4) 50RTC+H; ×4 objective, stained with Hematoxylin and Eosin (H&E), Alcian Blue (A-Blue), Collagen II (COL2) and SOX9. At week 4 cross-section for (A5) 50CC, (B5) 50CC+H and (C5) 50RTC+H; H&E staining, x4 objective. Chondrocyte morphology after 28 days hBM-MSCs differentiation, ×25 objective: H&E and A-Blue staining for (A1.1-A2.2) 50CC, (B1.1-B2.2) 50CC+H, (C1.1-C2.2) 50RTC+H scaffolds, (D1-D2) spheroid control, and (D1.1-D2.2) human femoral head cartilage.

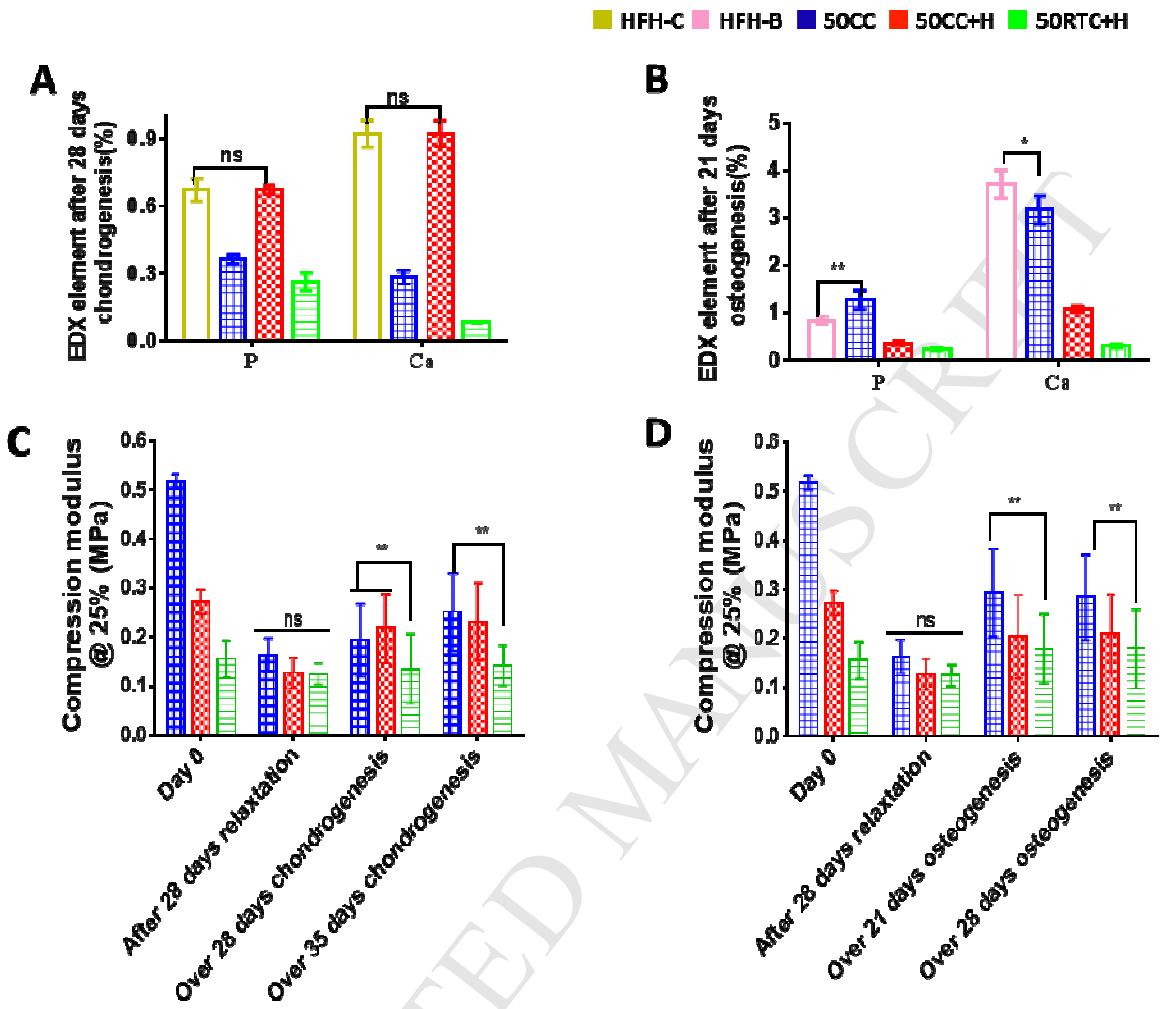

Figure 6 EDX quantification and compression mechanical properties of hBM-MSC seeded on the scaffolds after *in vitro* differentiation. (A-B) EDX analysis quantification of calcium and phosphorous after *in vitro* differentiation. (C-d) Mechanical compression modulus and strength after day 28 and day 35 chondrogenesis and day 21 and day 28 osteogenesis of hBM-MSCs compared to the cell-free scaffolds of day 0 and day 28 stiffness relaxation. *p<0.05; **p<0.01.

3.4 "Stiffness memory" effect on *in vitro* osteogenesis of hBM-MSCs

hBM-MSCs were also seeded on the three types of scaffolds and cultured with osteogenic differentiation medium to induce osteogenic differentiation, and RNA was collected over 4 weeks. Confocal microscopic images of immunofluorescent stained osteocyte-like mesenchymal cells cultured on the scaffolds for 21 days show strong positivity for collagen I (green), collagen II (blue) and calcium (red) deposition on the 50CC and 50CC+H scaffolds, followed by the 50RTC+H scaffold with a drastic reduction in the presence of calcium (**Figure 7 A-F**). More intriguingly, the intensity changes of overlapped green, blue and red at different focused layers of the 50CC and 50CC+H scaffolds provided evidence that osteogenic differentiation occurred within the scaffold frame at different depths, confirming cell penetration through to the scaffold construct core (**Figure 7 K-N**). The locally orientated mixed colourful interference fringes along

the scaffold strut (**Figure 7 A, B, D, E**) and concentric patterns around the printed pore (**Figure 7 A-B**) suggested preference for the alignment collagen fibres and mineralization during ossification guided by 3D printed micro-channels, reminiscent of osteon-like microscopic columns in lamellar bone. Deposition of calcium in the scaffolds was corroborated by quantification of the calcium content area surrounding collagen (**Figure 7 G**), and further evaluated in terms of alkaline phosphatase (ALP) activity and Alizarin red (ARS) (**Figure 7 H-I**). ALP is an early-stage marker of osteogenic differentiation and precursor to calcium deposition. ALP activity gradually increased with time in all scaffold groups, but greater expression of ALP was observed in the 50CC sample ($p<0.001$) followed by the 50CC+H and 50RTC+H groups after 3 weeks of culture. On the other hand, calcium deposition is a late-stage marker of osteogenic differentiation and can be evaluated in terms of ARS. ARS gradually increased as well in all sample groups after 3 weeks. In particular, 50CC scaffolds stained with higher ARS content compared to the rest of the groups ($p<0.0001$).

The expression levels of several key regulators of osteogenic differentiation were also quantified using qPCR (**Figure 7 J-O**). The levels of all genes tested gradually increased with time in terms of osterix, alkaline phosphatase, Collagen I, alpha-1 and osteopontin expression. It is noted that the increase on the 50RTC+H scaffold was slowed down after 2 weeks of culture. Gene expression levels peaked at week 3, with successful osteogenic differentiation occurring within the first 21 days. 50CC scaffolds exhibited significantly ($p<0.001$) higher mean relative expression levels of all studied genes compared to the rest of the scaffold groups and the spheroid controls. Furthermore, osteogenic associated gene expression in the 50CC scaffold after 3 weeks differentiation was comparable to that of HFH used as control (p-values non-significant) (**Figure 7 P**). The 50RTC+H scaffold expressed the lowest at all day points. Presence of Collagen I and osteocalcin released into the medium was further quantified by ELISA (**Figure 7 Q-R)**. In particular, the 50CC scaffold expressed the highest levels of Collagen I and osteocalcin over a 3-week period compared to the rest of the groups ($p<0.001$), and non-significant differences were quantified compared to HFH. These analyses were confirmed by histological staining in terms of Collagen I and ARS deposition (**Figure 8, Figure D5** in Data in Brief [43]) that highlighted differences between the samples. Stained 50RTC+H samples did not reveal much osteocyte-like matrix after 21 days of culture. Increased cellular penetration into the 50CC scaffold, alongside deposition of bone-like protein components of the extracellular matrix associated with osteogenesis were predominantly observed in the 50CC group compared to the rest of the groups relative to the spheroid control and human femoral head bone control. Furthermore, for verification of calcium, EDX mapping was used to confirm scaffold calcium accumulations (**Figure 6 B**, **Figure D4 B** and **Table D6** in Data in Brief [43]). EDX mapping detected the presence of carbon, phosphorus, calcium and silicon in the deposited accumulations after 21 days. High levels of Ca on the 50CC scaffolds (2.66 wt%) were observed compared to those in the 50CC+H and 50RTC+H groups (1.48wt % and 0.29 wt% respectively). For the human femoral head bone control (**Figure 6 B**, **Figure D4 D** in Data in Brief [43]), up to 3.72 wt% of Ca was quantified.

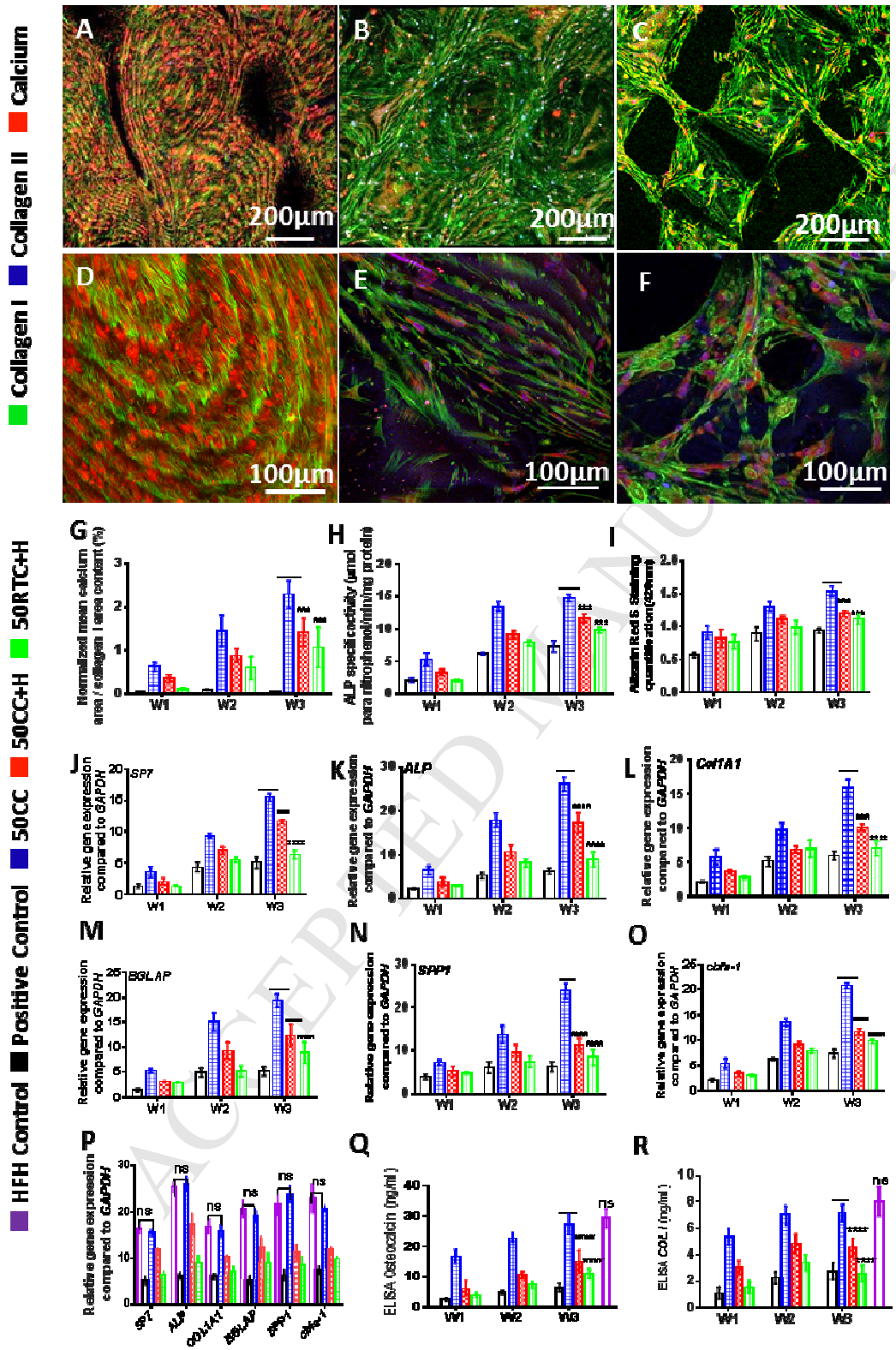

Figure 7 Osteogenic differentiation on 50% infill elastomer nanohybrid scaffolds during stiffness softening. (A-F) Confocal microscopy of hBM-MSCs under osteogenic conditions at

two different magnifications: osteogenic differentiation after 21 days for (A, D) 50CC, (B, E) 50CC+H, and (C, F) 50RTC+H showing Collagen 1 (green), Collagen II (blue) and calcium (red) deposition. Quantification of (G) calcium content surrounding Collagen, (H) alkaline phosphatase (ALP) activity and (I) Alizarin red S (ARS) staining for 50CC, 50CC+H and 50RTC+H scaffolds after 21 days. (J-O) Osteogenesis differentiation of hBM-MSCs quantified by qPCR during a 4-week period: comparative analysis for (J) *SP7* (Osteorix) expression; (K) *ALP* (alkaline phosphatase) expression; (L) *COL1A1* (Collagen I) expression; (M) *BGLAP* (Osteocalcin) expression; (N) *SPP1* (Osteopontin) expression and (O) *RUNX2* (cbfa-1) expression. (P) Comparison of quantitative analysis of gene expression at week 4 with human femoral head. (Q-R) ELISA analysis for presence of Osteocalcin and Collagen I secretion at weeks 1, 2 and 3. The mean of triplicate wells is plotted, and the error bars represent SD. ***p<0.001; ****p<0.0001; referenced with respect to CC sample " - ".

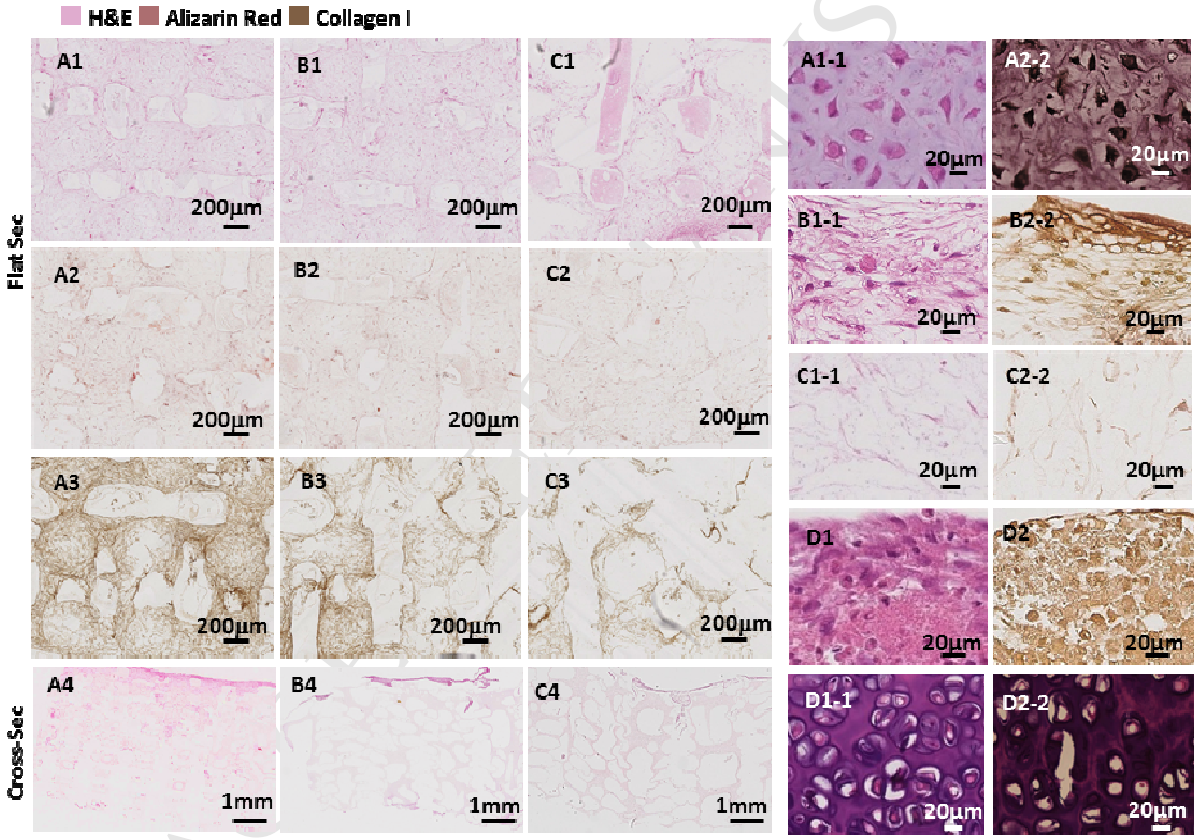

Figure 8 Histological analysis of osteogenic differentiation on 50% infill elastomer nanohybrid scaffolds during stiffness softening. At week 4 in plane-section for (A1-A3) 50CC, (B1-B3) 50CC+H; and (C1-C3) 50RTC+H; ×4 objective, stained with H&E, Collagen I (COL1) and Alizarin red. At week 4 cross-section for (A4) 50CC, (B4) CC+H and (C4) 50RTC+H; ×1.5 objective, H&E staining. Osteocyte morphology after 21 days hBM-MSCs differentiation; ×25 objective, H&E and Alizarin red staining for (A1.1-A2.2) 50CC, (B1.1-B2.2) 50CC+H, (C1.1-C2.2) 50RTC+H scaffolds, (D1-D2) spheroid control, and (D1.1-D2.2) human femoral head cartilage.

Cell-laden scaffolds were also evaluated after *in vitro* differentiation of hBM-MSCs in terms of their compression mechanical properties (**Figure 6C-D**). Increase compression moduli were observed within the scaffold groups after chondrogenic and osteogenic differentiation compared to cell-free scaffolds at day 0 and day 28 post-incubation at 37°C. It is interesting that the compression modulus of 50CC groups finally exceeded 50CC+H group after extended 35-day chondrogenic differentiation (Figure 6C).

4. Discussion

The work presented here suggests promise for the application of novel 3D-TIPS indirectly printed thermoresponsive "stiffness memory" elastomer scaffolds in tissue engineering applications. A simple dynamic system with stiffness changes has been developed, based on physical phase-transition and self-assembling of macromolecular chains in an inversely 3D-printed framework [41], rather than conventional hydrogel systems generated via chemical crosslinking [17,19,21–33]. This has been successfully applied to study the response and differentiation of stem cells in micro-niches. Starting stiffness and stiffness relaxation of the scaffolds can be modulated by the processing conditions (cryo-coagulation CC, cryo-coagulation and heating CC+H, and room temperature coagulation and heating RTC+H) (**Figure 1**). PUU-POSS scaffolds relaxed to their intrinsic soft hyperelasticity when subjected to body temperature due to a relaxation of the crystalline phase of the soft segments of PUU chains without changing its molecular structure. This system has been used to study chondrogenesis and osteogenesis of hBM-MSCs during stiffness relaxation. The observed slow stiffness softening of the scaffolds at mammalian physiological body temperatures is reminiscent of the slow relaxation of soft native tissue and of post-surgical tissue healing.

4.1 Tunable "stiffness memory" of the scaffolds

Variations in the infill density were found to affect the mechanical properties of the scaffolds, with overall greater compressive stiffness and strength for higher infill densities (**Figure 1 C**). In addition, 3D-TIPS of the scaffolds (CC group) exhibited overall the highest compressive mechanical properties compared to the CC+H and RTC+H groups with thermal treatment regardless of the infill density. This can be explained in terms of an ordered crystal lattice structure in the CC scaffolds and more crystal formation within the soft segment chains of their PUU [41], compared to a quasi-random nanophase amorphous structure in the RTC+H and CC+H group with little crystalline domains left due to temperature variations during the coagulation process and post thermal treatment. Isothermal relaxation of the static compression properties (**Figure 1D**) and dynamic cyclic tests (**Figure 2**) of the scaffolds further proved the different levels of stiffness softening of the scaffolds at body temperature, depending on their initial stiffness produced at different thermal process conditions. Such viscoelastic behaviour is attributed to the phase transition of melting crystalline domains and subsequent self-assembling of nanophase structure, with the CC scaffold exhibiting the greatest reduction (69%) by 28 days. No matter their thermal history and resulting in different initial stiffness, PUU-POSS scaffolds are bound to "remember" to relax to their intrinsic hyperelastic rubber phase (**Figure 1D** and **Figure 2**) when subjected to body temperature, close to the melting temperature of the soft segments (T_m=45°C). This stiffness 'memory' is in principle thermodynamically reversible despite it may be kinetically slow, which is of reminiscent biological tissue relaxation and

remodeling process.

This manufacturing versatility lends bio-mimicry to our products, for example approximating characteristics of human soft tissues. For instance, femoral non-mineralized and mineralized fibrocartilage exhibit compressive Young's moduli in the range 0.55-0.80 MPa and 0.20-0.60 MPa respectively [47] for the femoral and tibial condyles. The compressive modulus of the human ear cartilage is in the range 0.06-2.10 MPa [48–51], whilst human costal cartilage three-point bending values are 5–7 MPa [52]. Bone ECM has a high non-mineralized collagen content with compressive stiffness values of 0.1-1 MPa depending on stage of osteoid mineralization [34,53]. Prior to their stiffness relaxation, the fabricated scaffolds reached maximum compression modulus and strength of 0.80 - 0.10 MPa upon the infill density and coagulation processing, making them worthy of some consideration for cartilage tissue engineering applications such as joint capsule articular or ear cartilage, and potentially, non-load bearing bone engineering. Furthermore, thermoresponsive scaffolds offer an interesting opportunity as an *in vitro* model system to explore their effect of stiffness relaxation on host cells.

Ease of handling during surgery is an essential feature of any implant, and the dynamic nature of tissues should be replicated for enhanced tissue regeneration. Here again, there is room for further work, since our material exhibited stiffer mechanical support under typical surgical conditions, whilst relaxing their stiffness during typical remodeling physiological conditions. The major relaxation event occurred between 7 and 14 days post-incubation for 50CC and 50CC+H groups (**Figure 1D**), whilst at 28 day's incubation all groups relaxed to their intrinsic elasticity, reaching fairly uniform values. The "stiffness memory" effect of the scaffolds was also accelerated by cyclic loading tests after over 200,000 cycle under 25% larger compression strain within three days (**Figure 2D-I**).

4.2 "Stiffness memory" effect on *in vitro* differentiation of hBM-MSCs

Understanding stem cell plasticity *in vitro* is important because hBM-MSCs are a widely used cell source for regenerative medicine clinical trials. Stem cells in different states respond differentially as they commit to a specific fate, and their physical environment critically influences this process [14].

The differentiation of hBM-MSCs showed different preference of the initial stiffness and stiffness softening, resulting in enhanced chondrogenesis on the softer scaffold and osteogenesis on the stiffer one. The systematic tests and analysis demonstrated that chondrogenesis was promoted to a greater extent on the 50CC+H scaffold (**Figures 3-4**), while the 50CC group promoted greater osteogenic differentiation instead (**Figures 6-7**) following exposure of the cells to chondrogenic and osteogenic media respectively. The subsequent stiffness relaxation period over 28 days stimulated more osteogenic activity than chondrogenesis of hBM-MSCs cultured *in vitro*. The low initial stiffness and porous structure of the 50CC+H scaffold appeared to promote more chondrogenesis of hBM-MSCs, compared to the rigid 50CC scaffold with similar porous structure and soft 50RTC+H one with less micro- and nano-pores. The differences associated the gene expression between 50CC and 50CC+H became less significant by week 3 to 4, which may be attributed to enhanced cell attachment, migration and proliferation during the fast reduction of stiffness in the 50CC sample within the first two weeks of the chondrogenic culture. As more MSCs grew inside of the printed channels of the scaffold, their differentiation potential was presumed to be regulated by the cell-derived matrix microenvironment generated by earlier differentiated MSCs, which were guided by the scaffold substrate in the early first two weeks. In

addition, 50RTC remained the lowest gene expression compared to 50CC and 50CC+H despite its initial low stiffness, indicating another influential role of micro- and nano-porous structure of the scaffolds on promoting chondrogenesis. Therefore, it is hypothesized that chondrogenesis of hBM-MSCs is well-maintained on 50CC+H scaffolds due to a combination of a softer matrix with hierarchical porous structure that provided its highest surface area to volume ratio and specific guides and boundaries for cells to initially attach and growth, stimulating cartilage-like integrin mediators and offering a suitable framework for local cell adhesion and proliferation on this type of scaffold (**Figure 3).** In turn, this may have promoted cell penetration and proliferation into the scaffold core throughout the stiffness relaxation period, with the evidence of superior compression modulus of 50CC-based constructs after an extended differentiation post stiffness softening (**Figure 6C**).

On the other hand, the high initial stiffness of the 50CC scaffold and a more profound stiffness relaxation effect induced more osteogenesis. In contrast to chondrogenesis, osteogenesis was mainly dependent on the high initial stiffness and more profound relaxation effect provided by the 50CC porous scaffold with the evidence of the highest associated gene expression among the three types of scaffolds at all time points over 21 days (**Figure 7**). 3D printed microchannels appeared to guide the formation of the osteon-like lamellar structure during ossification with the highest mineralization in the 50CC (**Figures D4-D5** and **Table D6** in Data in Brief [43]). Although the scaffold already became softer within the first two weeks of relaxation, osteogenesis remained active and reached the peak on 21 to 28 days (**Figure 6D**), which may indicate the 'mechanical memory' of the hBM-MSC osteogenesis on rigid substrates. Integrins are known regulators of stem cell differentiation and an α2-integrin-ROCK-FAKERK1/2 axis was stimulated by the rigid matrices to promote RUNX2 activity, eventually leading to osteogenic fate [54]. In the osteogenic differentiation, it is envisaged that that MSCs were guided by the initial stiffness of the 50CC scaffold with enhanced local adhesion of mediated specific integrins on MSCs, activated RUNX2 expression through bone morphogenetic protein (BMP) pathway, leading to bone formation. During the subsequent stiffness softening, with more MSC migrated, proliferated and differentiated into the scaffold in the first 10 days (**Figure 3**), the original mechanosensing of the MSC may have gradually shifted to *de novo* cell-derived matrix sensing in more physiologically relevant 3D microenvironment generated by MSCs themselves within the printed channels, demonstrating resilient cellular 'mechanical memory' regardless the reduction of the stiffness. Besides, the difference of associated bone gene expression in 50CC+H and 50RTC+H remained despite non-significance, reflecting again the effect of porous structure. Clearly, the influence of the initial stiffness and stiffness softening on the MSC osteogenisis was predominant. Overall, these results appear to show that controlling stiffness and porosity thermally during manufacturing, along with an introduced substrate "stiffness memory" mechanism, significantly affects *in vitro* differentiation of hBM-MSCs.

Even when the matrix softened at body temperature (**Figure 1**) towards the intrinsic elasticity of the matrix, hBM-MSCs retained their "stemness commitment". This cellular "mechanical memory effect" has been previously reported, wherein mechanical properties of the substrate influenced cellular states in a manner that retained their specific activity while the matrix softened [17–20]. Analysis of the compressive mechanical properties of the scaffolds after *in vitro* hBM-MSC osteogenesis and chondrogenesis (**Figure 6 C-D**) demonstrated that a substantial component of the resulting stiffness may be attributed to cell-derived ECM [55,56], especially in those scaffolds where increase hBM-MSCs differentiation occurred (i.e. 50CC for osteogenesis and 50CC+H for chondrogenesis). For the extended longer differentiation, the

softest 50RTC+H scaffold group with less porous structure and dense smooth surface remained stable with no obvious changes within the period of tests, and represented the least efficient differentiation. The soft and porous 50CC+H group showed a slight relaxation in the modulus with noticeable enhancements of the resting scaffold mechanical properties, attributed by the most efficient chondrogenesis guided *via* both porous structure and soft stiffness. Despite being relatively slow in the early stages of proliferation and chondrogenesis compared to 50CC+H, the outstanding mechanical performance of the 50CC group may be mainly attributed to "stiffness memory". Therefore, porous structure and surface morphology may be the predominant regulator in the early stage of chondrogenesis differentiation. In osteogenic culture, the initial stiffness appeared to be the determining regulator for governing the osteogenic lineage in the beginning, and pronounce stiffness relaxation enhanced the efficiency of bone formation. Overall, only cryo-3D-TIPS (50CC) scaffolds retained the full range of novel advantages in terms of proliferation and differentiation capabilities for hBM-MSCs, and this would be the preferred family member for further research towards possible clinical application.

5. Conclusions

This study suggests that the transitional stiffness relaxation effect of a family of thermoresponsive stiffness scaffolds significantly influence hBM-MSC proliferation and differentiation into the chondrogenic and osteogenic mesenchymal lineages. In the early stage of differentiation, stem cells seeded onto these scaffolds synthesize and promote deposition of cartilage-like and bone-forming proteins regulated by the initial stiffness and porous structure of the scaffold, and then appear to be favored by the subsequent "stiffness memory" effect exhibited by this intriguing family of materials. Stiffness softening enhances the efficiency of MSC growth and differentiation. As more MSCs grow within the 3D printed microchannel network, the differentiation signal pathway may switch from the initial substrate-mechanosensing to cell-derived matrix sensing in 3D microenvironment, accelerating the differentiation and leading to the maturation of the synthetic cartilage and bone tissue.

Through their tunable stiffness and stiffness relaxation, these hierarchical porous scaffolds represent a promising platform for the development of smart and biological responsive tissue-engineered implants and devices, with matched dynamic mechanical properties to suit a variety of different dynamic cell-lines, tissues and organs. Integrating a "stiffness memory" effect and a 3D printing approach can provide a valuable combinatorial tool for improved MSC growth and differentiation, making these scaffolds worthy of further consideration for future regenerative medicine and implantable devices through the development of biodegradable polyurethane and other elastomers. *In vivo* studies have been carried out to account for the stiffness softening effect of these scaffolds on subcutaneous tissue ingrowth, vascularization and inflammatory response, which will be featured in a future paper. More specific *in vivo* studies on the effect of stiffness softening in cartilage and bone models are deserved further investigation.

Acknowledgments
The authors acknowledge financial support by the Engineering and Physical Science Research Council (EPSRC grant no. EP/L020904/1, EP/M026884/1 and EP/R02961X/1).

Competing interests
The authors declare no potential conflict of interests with respect to the research, authorship and/or publication of this article.

References:

[1] Y. Wang, G. Wang, X. Luo, J. Qiu, C. Tang, Substrate stiffness regulates the proliferation, migration, and differentiation of epidermal cells, Burns J. Int. Soc. Burn Inj. 38 (2012) 414–420. doi:10.1016/j.burns.2011.09.002.

[2] M. Guvendiren, J.A. Burdick, Stiffening hydrogels to probe short- and long-term cellular responses to dynamic mechanics, Nat. Commun. 3 (2012) 792. doi:10.1038/ncomms1792.

[3] D.T. Butcher, T. Alliston, V.M. Weaver, A tense situation: forcing tumour progression, Nat. Rev. Cancer. 9 (2009) 108–122. doi:10.1038/nrc2544.

[4] T.R. Cox, J.T. Erler, Remodeling and homeostasis of the extracellular matrix: implications for fibrotic diseases and cancer, Dis. Model. Mech. 4 (2011) 165–178. doi:10.1242/dmm.004077.

[5] K.M. Ferlin, M.E. Prendergast, M.L. Miller, B.-N.B. Nguyen, D.S. Kaplan, J.P. Fisher, Development of a dynamic stem cell culture platform for mesenchymal stem cell adhesion and evaluation, Mol. Pharm. 11 (2014) 2172–2181. doi:10.1021/mp500062n.

[6] R. Olivares-Navarrete, E.M. Lee, K. Smith, S.L. Hyzy, M. Doroudi, J.K. Williams, K. Gall, B.D. Boyan, Z. Schwartz, Substrate Stiffness Controls Osteoblastic and Chondrocytic Differentiation of Mesenchymal Stem Cells without Exogenous Stimuli, PLOS ONE. 12 (2017) e0170312. doi:10.1371/journal.pone.0170312.

[7] J.H. Wen, L.G. Vincent, A. Fuhrmann, Y.S. Choi, K.C. Hribar, H. Taylor-Weiner, S. Chen, A.J. Engler, Interplay of matrix stiffness and protein tethering in stem cell differentiation, Nat. Mater. advance on (2014) 1–21. doi:10.1038/nmat4051.

[8] O. Chaudhuri, S.T. Koshy, C. Branco da Cunha, J.-W. Shin, C.S. Verbeke, K.H. Allison, D.J. Mooney, Extracellular matrix stiffness and composition jointly regulate the induction of malignant phenotypes in mammary epithelium, Nat. Mater. 13 (2014) 970–978. doi:10.1038/nmat4009.

[9] A. Pathak, S. Kumar, Independent regulation of tumor cell migration by matrix stiffness and confinement, Proc. Natl. Acad. Sci. U. S. A. 109 (2012) 10334–10339. doi:10.1073/pnas.1118073109.

[10] C.M. Lo, H.B. Wang, M. Dembo, Y.L. Wang, Cell movement is guided by the rigidity of the substrate, Biophys. J. 79 (2000) 144–152. doi:10.1016/S0006-3495(00)76279-5.

[11] E. Hadjipanayi, V. Mudera, R.A. Brown, Guiding cell migration in 3D: A collagen matrix with graded directional stiffness, Cell Motil. Cytoskeleton. 66 (2009) 121–128. doi:10.1002/cm.20331.

[12] E. Hadjipanayi, V. Mudera, R.A. Brown, Close dependence of fibroblast proliferation on collagen scaffold matrix stiffness, J. Tissue Eng. Regen. Med. 3 (2009) 77–84. doi:10.1002/term.136.

[13] J.P. Winer, P.A. Janmey, M.E. McCormick, M. Funaki, Bone marrow-derived human mesenchymal stem cells become quiescent on soft substrates but remain responsive to chemical or mechanical stimuli, Tissue Eng. Part A. 15 (2009) 147–154. doi:10.1089/ten.tea.2007.0388.

[14] A.J. Engler, S. Sen, H.L. Sweeney, D.E. Discher, Matrix elasticity directs stem cell lineage specification, Cell. 126 (2006) 677–689. doi:10.1016/j.cell.2006.06.044.

[15] A.J. Keung, E.M. de Juan-Pardo, D.V. Schaffer, S. Kumar, Rho GTPases mediate the mechanosensitive lineage commitment of neural stem cells, Stem Cells Dayt. Ohio. 29 (2011) 1886–1897. doi:10.1002/stem.746.

[16] M. Targosz-Korecka, G.D. Brzezinka, K.E. Malek, E. Stępień, M. Szymonski, Stiffness memory of EA.hy926 endothelial cells in response to chronic hyperglycemia, Cardiovasc. Diabetol. 12 (2013) 96. doi:10.1186/1475-2840-12-96.

[17] A.A. Abdeen, J. Lee, N.A. Bharadwaj, R.H. Ewoldt, K.A. Kilian, Temporal Modulation of Stem Cell Activity Using Magnetoactive Hydrogels, Adv. Healthc. Mater. 5 (2016) 2536–2544. doi:10.1002/adhm.201600349.

[18] P.M. Gilbert, K.L. Havenstrite, K.E.G. Magnusson, A. Sacco, N.A. Leonardi, P. Kraft, N.K. Nguyen, S. Thrun, M.P. Lutolf, H.M. Blau, Substrate Elasticity Regulates Skeletal Muscle Stem Cell Self-Renewal in Culture, Science. 329 (2010) 1078–1081. doi:10.1126/science.1191035.

[19] C. Yang, M.W. Tibbitt, L. Basta, K.S. Anseth, Mechanical memory and dosing influence stem cell fate, Nat. Mater. 13 (2014) 645–652. doi:10.1038/nmat3889.

[20] J. Lee, A.A. Abdeen, K.A. Kilian, Rewiring mesenchymal stem cell lineage specification by switching the biophysical microenvironment, Sci. Rep. 4 (2014) 5188. doi:10.1038/srep05188.

[21] S.R. Caliari, M. Perepelyuk, E.M. Soulas, G.Y. Lee, R.G. Wells, J.A. Burdick, Gradually softening hydrogels for modeling hepatic stellate cell behavior during fibrosis regression, Integr. Biol. Quant. Biosci. Nano Macro. 8 (2016) 720–728. doi:10.1039/c6ib00027d.

[22] B.M. Gillette, J.A. Jensen, M. Wang, J. Tchao, S.K. Sia, Dynamic hydrogels: switching of 3d microenvironments using two-component naturally derived extracellular matrices, Adv. Mater. 22 (2010) 686–691. doi:10.1002/adma.200902265.

[23] R.S. Stowers, S.C. Allen, L.J. Suggs, Dynamic phototuning of 3D hydrogel stiffness, Proc. Natl. Acad. Sci. U. S. A. 112 (2015) 1953–1958. doi:10.1073/pnas.1421897112.
[24] F.X. Jiang, B. Yurke, R.S. Schloss, B.L. Firestein, N.A. Langrana, Effect of dynamic stiffness of the substrates on neurite outgrowth by using a DNA-crosslinked hydrogel, Tissue Eng. Part A. 16 (2010) 1873–1889. doi:10.1089/ten.TEA.2009.0574.
[25] D.C. Lin, B. Yurke, N.A. Langrana, Inducing reversible stiffness changes in DNA-crosslinked gels, J. Mater. Res. 20 (2005) 1456–1464. doi:10.1557/JMR.2005.0186.
[26] D.C. Lin, B. Yurke, N.A. Langrana, Mechanical properties of a reversible, DNA-crosslinked polyacrylamide hydrogel, J. Biomech. Eng. 126 (2004) 104–110.
[27] F.X. Jiang, B. Yurke, R.S. Schloss, B.L. Firestein, N.A. Langrana, The relationship between fibroblast growth and the dynamic stiffnesses of a DNA crosslinked hydrogel, Biomaterials. 31 (2010) 1199–1212. doi:10.1016/j.biomaterials.2009.10.050.
[28] Y. Lei, D.V. Schaffer, A fully defined and scalable 3D culture system for human pluripotent stem cell expansion and differentiation, Proc. Natl. Acad. Sci. 110 (2013) E5039–E5048. doi:10.1073/pnas.1309408110.
[29] H.Y. Yoshikawa, F.F. Rossetti, S. Kaufmann, T. Kaindl, J. Madsen, U. Engel, A.L. Lewis, S.P. Armes, M. Tanaka, Quantitative evaluation of mechanosensing of cells on dynamically tunable hydrogels, J. Am. Chem. Soc. 133 (2011) 1367–1374. doi:10.1021/ja1060615.
[30] J.L. Young, A.J. Engler, Hydrogels with time-dependent material properties enhance cardiomyocyte differentiation in vitro, Biomaterials. 32 (2011) 1002–1009. doi:10.1016/j.biomaterials.2010.10.020.
[31] Ubaidillah, J. Sutrisno, A. Purwanto, S.A. Mazlan, Recent Progress on Magnetorheological Solids: Materials, Fabrication, Testing, and Applications, Adv. Eng. Mater. 17 (2015) 563–597. doi:10.1002/adem.201400258.
[32] T. Mitsumata, S. Ohori, A. Honda, M. Kawai, Magnetism and viscoelasticity of magnetic elastomers with wide range modulation of dynamic modulus, Soft Matter. 9 (2012) 904–912. doi:10.1039/C2SM26717A.
[33] M. Mayer, R. Rabindranath, J. Börner, E. Hörner, A. Bentz, J. Salgado, H. Han, H. Böse, J. Probst, M. Shamonin, G.J. Monkman, G. Schlunck, Ultra-Soft PDMS-Based Magnetoactive Elastomers as Dynamic Cell Culture Substrata, PLOS ONE. 8 (2013) e76196. doi:10.1371/journal.pone.0076196.
[34] A.J. Engler, S. Sen, H.L. Sweeney, D.E. Discher, Matrix Elasticity Directs Stem Cell Lineage Specification, Cell. 126 (2006) 677–689. doi:10.1016/j.cell.2006.06.044.
[35] J. Pelham, Robert J., Y.-L. Wang, Cell locomotion and focal adhesions are regulated by substrate flexibility, Proc. Natl. Acad. Sci. U. S. A. 94 (1997) 13661–13665. doi:10.1073/pnas.94.25.13661.
[36] T. Yeung, P.C. Georges, L.A. Flanagan, B. Marg, M. Ortiz, M. Funaki, N. Zahir, W. Ming, V. Weaver, P.A. Janmey, Effects of substrate stiffness on cell morphology, cytoskeletal structure, and adhesion, Cell Motil. Cytoskeleton. 60 (2005) 24–34. doi:10.1002/cm.20041.
[37] J.H. Wen, L.G. Vincent, A. Fuhrmann, Y.S. Choi, K.C. Hribar, H. Taylor-Weiner, S. Chen, A.J. Engler, Interplay of matrix stiffness and protein tethering in stem cell differentiation, Nat. Mater. advance on (2014) 1–21. doi:10.1038/nmat4051.
[38] S. Kumar, Cellular mechanotransduction: Stiffness does matter, Nat. Mater. 13 (2014) 918–920. doi:10.1038/nmat4094.
[39] M. Guvendiren, J. a Burdick, Stiffening hydrogels to probe short- and long-term cellular responses to dynamic mechanics., Nat. Commun. 3 (2012) 792. doi:10.1038/ncomms1792.
[40] A. Pathak, S. Kumar, Biophysical regulation of tumor cell invasion: moving beyond matrix stiffness., Integr. Biol. Quant. Biosci. Nano Macro. 3 (2011) 267–278. doi:10.1039/c0ib00095g.
[41] L. Wu, J. Virdee, E. Maughan, A. Darbyshire, G. Jell, M. Loizidou, M. Emberton, P. Butler, A. Howkins, A. Reynolds, I. Boyd, M. Birchall, W. Song, 3D printing guided stiffness memory elastomer nanohybrid scaffolds for biologically responsive bespoke soft implants, Acta biomaterialia (in press). (2018).
[42] R.Y. Kannan, H.J. Salacinski, M. Odlyha, P.E. Butler, A.M. Seifalian, The degradative resistance of polyhedral oligomeric silsesquioxane nanocore integrated polyurethanes: An in vitro study, Biomaterials. 27 (2006) 1971–1979. doi:10.1016/j.biomaterials.2005.10.006.
[43] L. Wu, A. Magaz, T. Wang, C. Liu, A. Darbyshire, M. Loizidou, M. Emberton, M. Birchall, W. Song, Data of a stiffness softening mechanism effect on proliferation and differentiation of a human bone marrow derived mesenchymal stem cell line towards the chondrogenic and osteogenic lineages, Data in Brief (submitted). (2018).
[44] T. Hruz, M. Wyss, M. Docquier, M.W. Pfaffl, S. Masanetz, L. Borghi, P. Verbrugghe, L. Kalaydjieva, S. Bleuler, O. Laule, P. Descombes, W. Gruissem, P. Zimmermann, RefGenes: identification of reliable and

condition specific reference genes for RT-qPCR data normalization, BMC Genomics. 12 (2011) 156. doi:10.1186/1471-2164-12-156.
[45] C.A. Gregory, W. Grady Gunn, A. Peister, D.J. Prockop, An Alizarin red-based assay of mineralization by adherent cells in culture: comparison with cetylpyridinium chloride extraction, Anal. Biochem. 329 (2004) 77–84. doi:10.1016/j.ab.2004.02.002.
[46] N. Wang, K. Burugapalli, W. Song, J. Halls, F. Moussy, Y. Zheng, Y. Ma, Z. Wu, K. Li, Tailored fibro-porous structure of electrospun polyurethane membranes, their size-dependent properties and trans-membrane glucose diffusion, J. Membr. Sci. 427 (2013) 207–217. doi:10.1016/j.memsci.2012.09.052.
[47] K.L. Moffat, W.-H.S. Sun, N.O. Chahine, P.E. Pena, S.B. Doty, C.T. Hung, G.A. Ateshian, H.H. Lu, Characterization of the mechanical properties and mineral distribution of the anterior cruciate ligament-to-bone insertion site, Conf. Proc. Annu. Int. Conf. IEEE Eng. Med. Biol. Soc. IEEE Eng. Med. Biol. Soc. Annu. Conf. 1 (2006) 2366–2369. doi:10.1109/IEMBS.2006.259299.
[48] K.A. Athanasiou, M.P. Rosenwasser, J.A. Buckwalter, T.I. Malinin, V.C. Mow, Interspecies comparisons of in situ intrinsic mechanical properties of distal femoral cartilage, J. Orthop. Res. Off. Publ. Orthop. Res. Soc. 9 (1991) 330–340. doi:10.1002/jor.1100090304.
[49] K.A. Athanasiou, A. Agarwal, F.J. Dzida, Comparative study of the intrinsic mechanical properties of the human acetabular and femoral head cartilage, J. Orthop. Res. Off. Publ. Orthop. Res. Soc. 12 (1994) 340–349. doi:10.1002/jor.1100120306.
[50] L. Zhang, J. Hu, K.A. Athanasiou, The role of tissue engineering in articular cartilage repair and regeneration, Crit. Rev. Biomed. Eng. 37 (2009) 1–57.
[51] M.F. Griffin, Y. Premakumar, A.M. Seifalian, M. Szarko, P.E.M. Butler, Biomechanical characterisation of the human auricular cartilages; implications for tissue engineering, Ann. Biomed. Eng. 44 (2016) 3460–3467. doi:10.1007/s10439-016-1688-1.
[52] A. Lau, M.L. Oyen, R.W. Kent, D. Murakami, T. Torigaki, Indentation stiffness of aging human costal cartilage, Acta Biomater. 4 (2008) 97–103. doi:10.1016/j.actbio.2007.06.008.
[53] K. Chatterjee, S. Lin-Gibson, W.E. Wallace, S.H. Parekh, Y.J. Lee, M.T. Cicerone, M.F. Young, C.G. Simon, The effect of 3D hydrogel scaffold modulus on osteoblast differentiation and mineralization revealed by combinatorial screening, Biomaterials. 31 (2010) 5051–5062. doi:10.1016/j.biomaterials.2010.03.024.
[54] Y.-R.V. Shih, K.-F. Tseng, H.-Y. Lai, C.-H. Lin, O.K. Lee, Matrix stiffness regulation of integrin-mediated mechanotransduction during osteogenic differentiation of human mesenchymal stem cells, J. Bone Miner. Res. Off. J. Am. Soc. Bone Miner. Res. 26 (2011) 730–738. doi:10.1002/jbmr.278.
[55] H.D. Kim, Y. Lee, Y. Kim, Y. Hwang, N.S. Hwang, Biomimetically Reinforced Polyvinyl Alcohol-Based Hybrid Scaffolds for Cartilage Tissue Engineering, Polymers. 9 (2017) 655. doi:10.3390/polym9120655.
[56] P.A. Levett, D.W. Hutmacher, J. Malda, T.J. Klein, Hyaluronic Acid Enhances the Mechanical Properties of Tissue-Engineered Cartilage Constructs, PLoS ONE. 9 (2014). doi:10.1371/journal.pone.0113216.